A 3′ terminal sugar-specific polymerase for terminator-free single-nucleotide extension of RNA oligonucleotides

Joonyoung Lee[1], Seong-Gyu Lee[2], Jin Young Kang[3*], and Ki Jun Jeong[1,4,5*]

[1] Department of Chemical and Biomolecular Engineering, KAIST, 291 Daehak-ro, Yuseong-gu, Daejeon 34141, Republic of Korea.

[2] KAIST Analysis Center for Research Advancement, KAIST, 291 Daehak-ro, Yuseong-gu, Daejeon 34141, Republic of Korea.

[3] Department of Chemistry, KAIST, 291 Daehak-ro, Yuseong-gu, Daejeon 34141, Republic of Korea.

[4] Graduate School of Engineering Biology, KAIST, 291 Daehak-ro, Yuseong-gu, Daejeon 34141, Republic of Korea.

[5] KAIST Institute for BioCentury, KAIST, 291 Daehak-ro, Yuseong-gu, Daejeon 34141, Republic of Korea.

*** To whom correspondence should be addressed:**

Email: kjjeong@kaist.ac.kr (KJ Jeong), jykang59@kaist.ac.kr (JY Kang)

TABLE OF CONTENTS

Supplementary Figures

SUPPLEMENTARY FIGURES

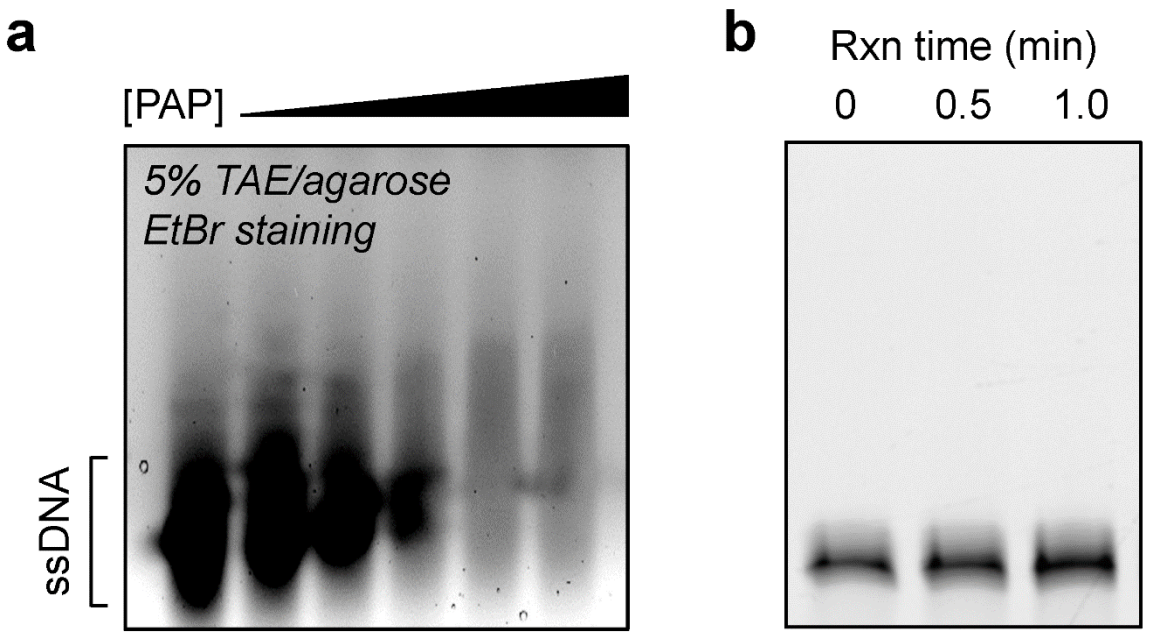

Supplementary Fig. 1 | *Ec*PAP forms a stable complex with single-stranded DNA (ssDNA) despite rejecting it as substrate
a, Gel shift assay using purified *Ec*PAP and a 68 nt unlabeled ssDNA oligonucleotide (5′-ATGCAAATAAGGCTATGCGATCAAATGTGTATGCAAATAAGGGCTTAGCTCCAATGCTG TATGCAAAT-3′). The *Ec*PAP-ssDNA mixture was incubated under low-salt conditions (50 mM MOPS-NaOH, 10 mM $MgCl_2$, pH 7.8) with varying levels of *Ec*PAP and resolved in a 5% TAE/agarose gel stained with ethidium bromide (EtBr). While the crude experimental setup produced vertically smeared bands, the resulting gel image was still clear enough to unambiguously detect dose-dependent mobility shifts in the ssDNA species upon addition of *Ec*PAP. **b,** *Ec*PAP-catalyzed primer extension assay using FAM-DNA (5′-ATAGAGAAGTATTACCAGCGGATGAGCTAGATGAGCTAGACGAAA-3′) and rATP. Denaturing PAGE analysis (12 × 10 cm TBE/Urea-PAGE) showed no detectable polyadenylation of the FAM-labeled ssDNA primer under the conditions assayed.

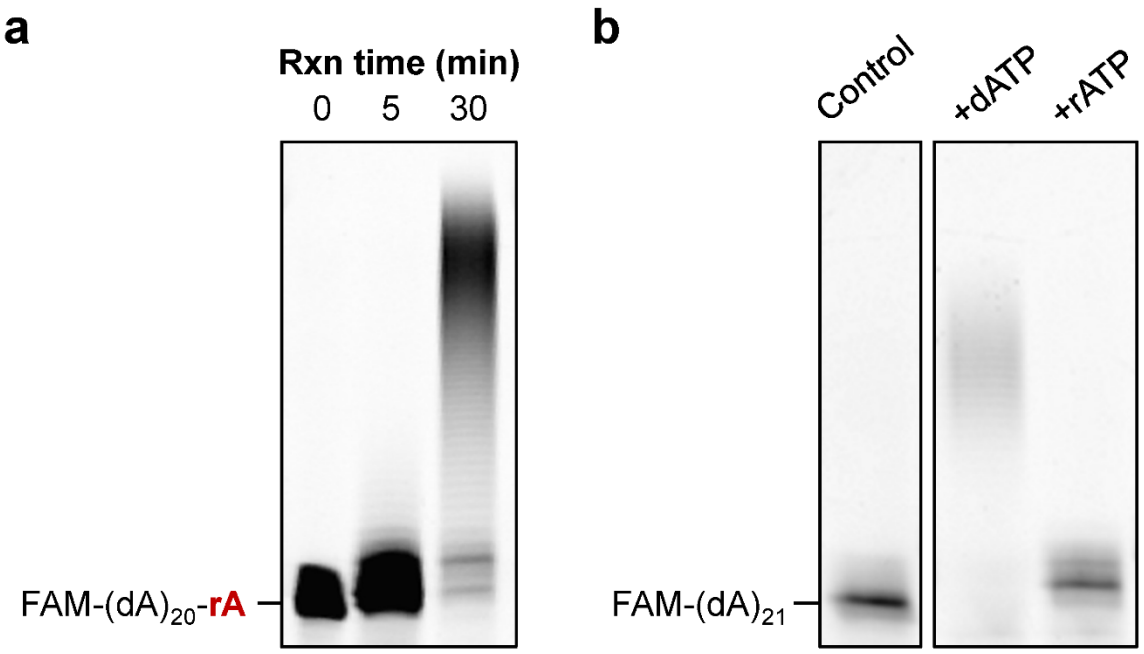

Supplementary Fig. 2 | *Bt*TdT exhibits minimal primer terminal sugar specificity
a, Time-course analysis of primer extension reaction of 3′ sugar-substituted DNA primer FAM-$(dA)_{20}$-rA (2.5 μM) by *Bt*TdT (2 U/μL) in the presence of excess dATP (1 mM). **b,** Extension of FAM-$(dA)_{21}$ (0.2 μM) by *Bt*TdT (2 U/μL) in the presence of dATP (1 mM) or rATP (1 mM). Reactions were each carried out for 15 min. The rATP reaction corresponds to a '*d*MIL-like' reaction for *Bt*TdT as a DNA primer (with preferred sugar) is extended with a ribo-NTP (with less preferred sugar). Reaction products in **a-b** were resolved on 12 × 10 cm 15% Urea-PAGE gels.

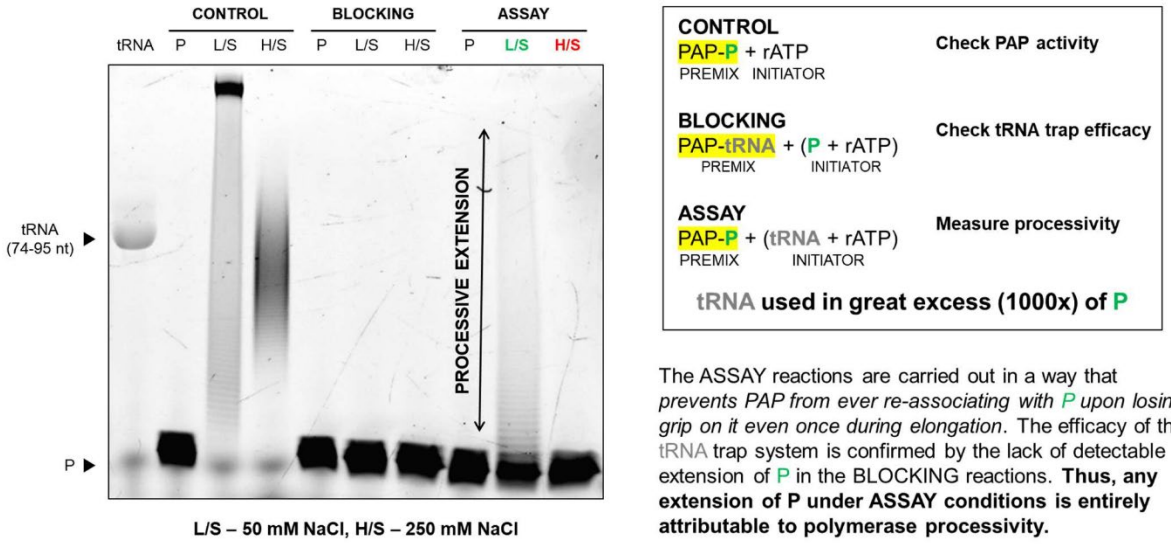

Supplementary Fig. 3 | *Ec*PAP exhibits significant processivity during polyadenylation that can be suppressed by high ionic strength

Results for "control", "blocking", and "assay" primer extension reactions carried out for determining the processivity of *Ec*PAP under low-salt (50 mM NaCl, "L/S") and high-salt (250 mM, "H/S") conditions **(see Supplementary Methods for detail)**. *tRNA* and *P* refer to unlabeled tRNA purified from *E. coli* MRE600 (*i.e.* the tRNA trap) and FAM-$(rA)_{21}$ RNA, respectively. Reaction products were resolved on a 12 × 10 cm 15% Urea-PAGE gel.

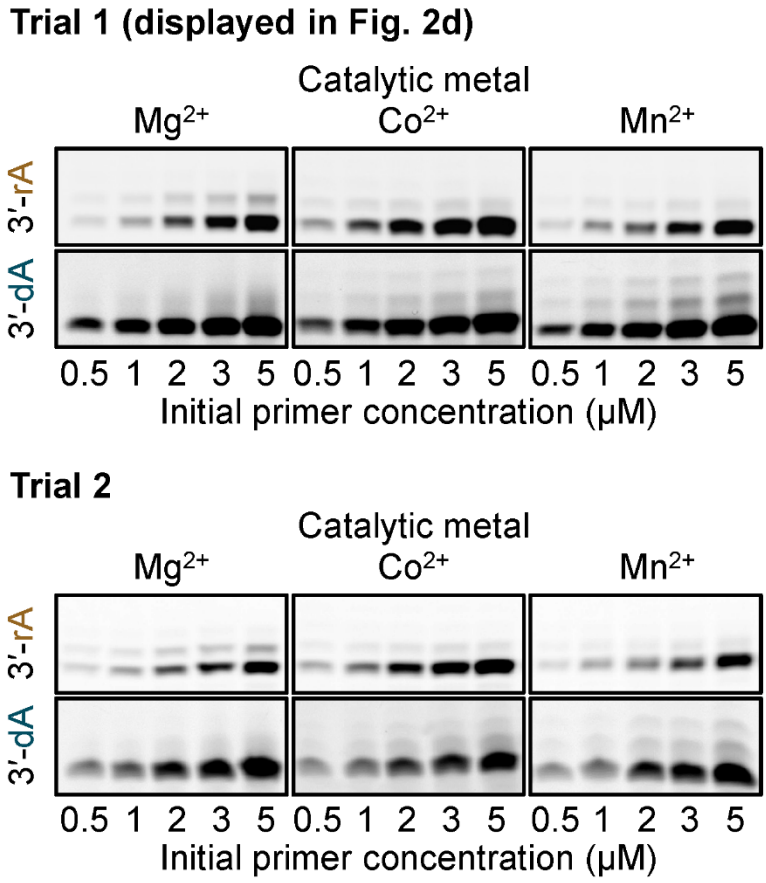

Supplementary Fig. 4 | Original gel results (showing both of the duplicate runs) for Fig. 2d-f

Steady-state primer extension reactions using FAM-$(rA)_{20}$-rA (3′-rA) and FAM-$(rA)_{20}$-dA (3′-dA) with different divalent metal cofactors (Mg^{2+}, Mn^{2+}, Co^{2+}). Here, we show the original results for both of the duplicate runs used for initial velocity estimation in **Fig. 2d-f**.

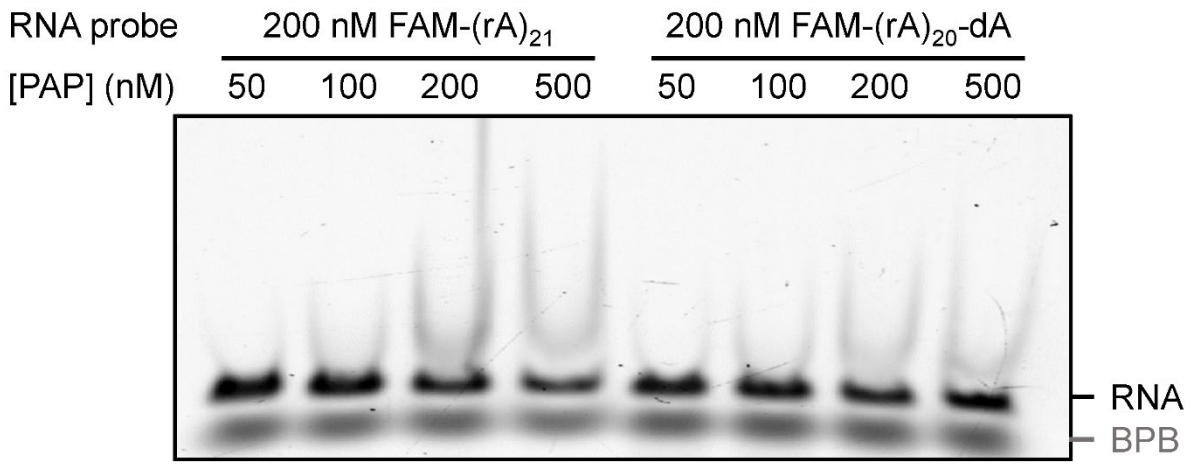

Supplementary Fig. 5 | Gel shift assays indicate comparable binding affinities of *Ec*PAP for FAM-$(rA)_{21}$ and FAM-$(rA)_{20}$-dA primers

Oligonucleotides FAM-$(rA)_{21}$ and FAM-$(rA)_{20}$-dA were each incubated with different levels of *Ec*PAP (50-500 nM) under low-salt conditions (<50 mM NaCl) for 15 min at room temperature and separated on a 12 × 10 cm 12% native TBE/PAGE gel. Labels 'RNA' and 'BPB' refer to unbound primers and the bromophenol blue dye front, respectively.

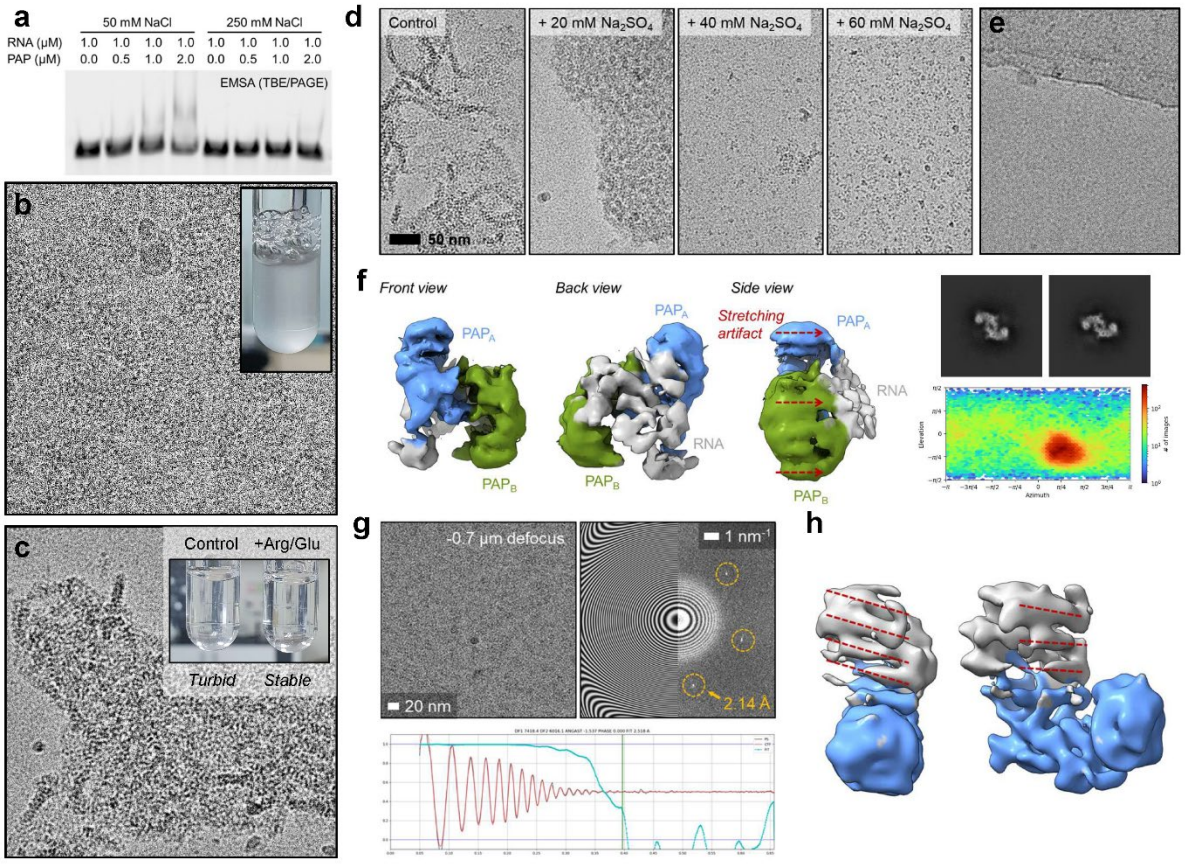

Supplementary Fig. 6 | Challenges in cryo-EM analysis of *Ec*PAP

a, Gel shift assay using FAM-$(rA)_{26}$ oligonucleotide and purified *Ec*PAP under low-salt (50 mM NaCl) and high-salt (250 mM NaCl) conditions. **b,** Representative cryo-EM micrograph of *Ec*PAP diluted in (low-salt) 50 mM MOPS-NaOH (pH 7.0) buffer. The inset image shows the physical state of the *Ec*PAP sample immediately after dilution. **c,** Representative cryo-EM micrograph of *Ec*PAP diluted in a low-salt buffer containing 50 mM L-Arg and 50 mM L-Glu. Inset images show the physical state of the *Ec*PAP sample immediately after dilution in a low-salt buffer with (right) and without (left) added L-Arg and L-Glu. **d,** Representative cryo-EM micrographs of *Ec*PAP diluted in a low-salt buffer containing 50 mM L-Arg and 50 mM L-Glu with different concentrations of added Na_2SO_4. **e,** Representative cryo-EM micrograph of *Ec*PAP diluted in a low-salt buffer containing 30 mM NaOAc. **f,** 3D reconstruction, 2D class averages, and orientation distribution of dimeric *Ec*PAP incubated with an RNA oligonucleotide and AMPCPP in a low-salt buffer containing 50 mM L-Arg, 50 mM L-Glu, and 20 mM Na_2SO_4. **g,** Representative motion-corrected, dose-weighted low-defocus micrograph and power spectrum from a Krios dataset collected from a graphene-coated *Ec*PAP-RNA-AMPCPP grid, showing graphene-derived reflections at 2.14 Å. **h,** 3D reconstruction of *Ec*PAP-RNA-AMPCPP from the same dataset, showing anisotropic resolution from preferred orientation.

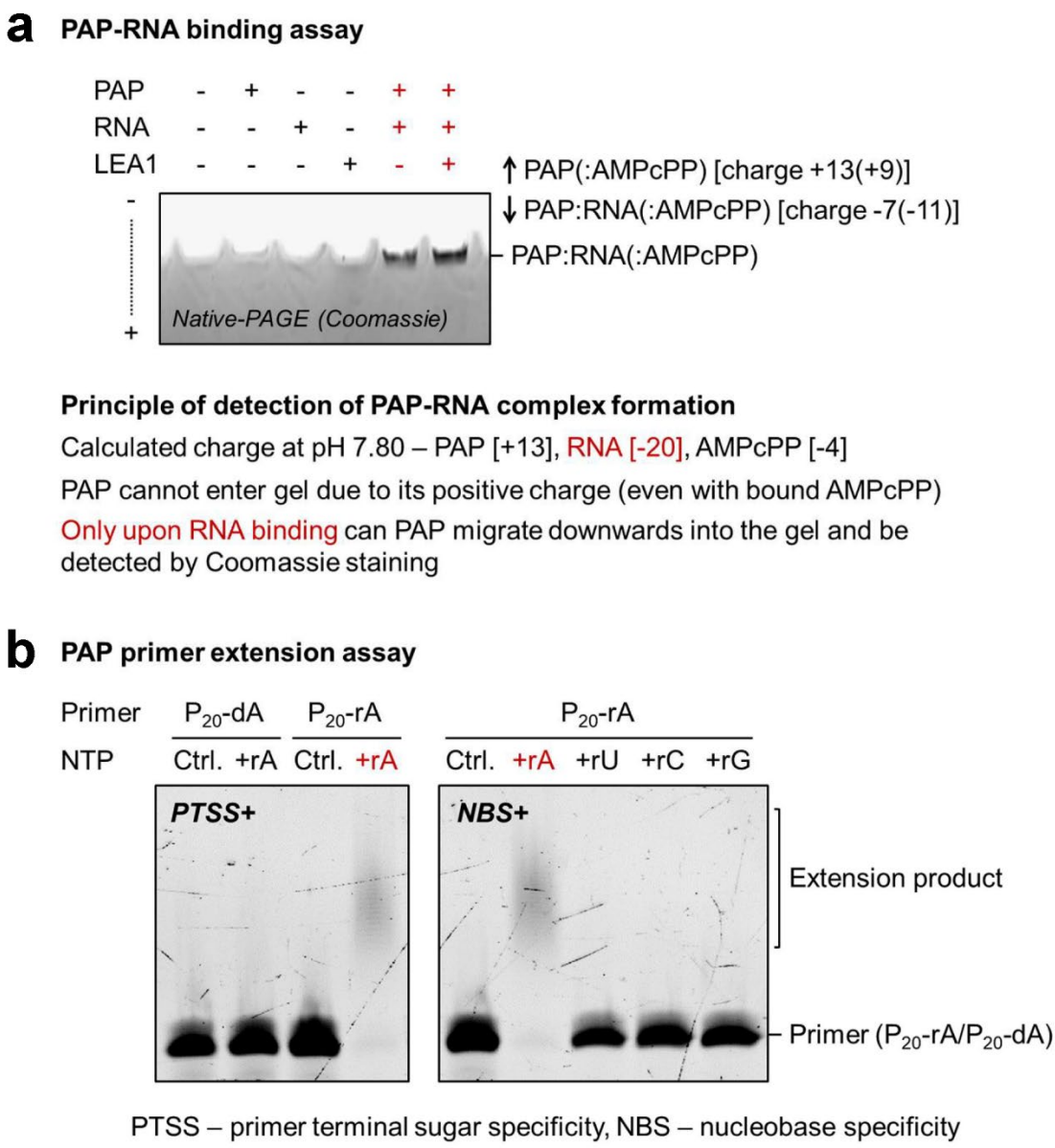

Supplementary Fig. 7 | *Ec*PAP is fully active and retains specificity under optimized buffer conditions

a, Modified gel shift assay confirming stable *Ec*PAP-RNA complex formation under optimized cryo-EM conditions. *Ec*PAP (~10 µM) was incubated on ice for >1 h with 50 µM $(rA)_{25}$ RNA, 5 mM AMPCPP, and 30 µM *Aav*LEA1 in binding buffer (50 mM Tris-Cl, 10 mM $MgCl_2$, 50 mM L-Arg, 50 mM L-Glu, 60 mM Na_2SO_4, pH 7.80). Control reactions omitting one or more components (*Ec*PAP, RNA, AMPCPP, or *Aav*LEA1) were analyzed in parallel. Mixtures were resolved on a 6% native TBE-PAGE gel and Coomassie-stained to visualize *Ec*PAP. Because of its large positive charge (+13) at the assay pH, free *Ec*PAP cannot enter the gel; migration into the gel is strictly dependent on the formation of a stable, negatively charged complex with RNA. **b,** *Ec*PAP primer extension assays to verify preservation of activity and nucleotide sugar/base specificities under optimized cryo-EM conditions. *Ec*PAP (~2 µM) was incubated with 1 µM FAM-$(rA)_{21}$ ("P_{20}-rA") or FAM-$(rA)_{20}$-dA ("P_{20}-dA), one of four rNTPs (N=A, U, C, or G), and 30 µM *Aav*LEA1 in binding buffer (as in **a**) at 37 °C for 1 min. Reactions were quenched using 2x SNL buffer and analyzed on a 12 × 10 cm 15% TBE/Urea-PAGE gel.

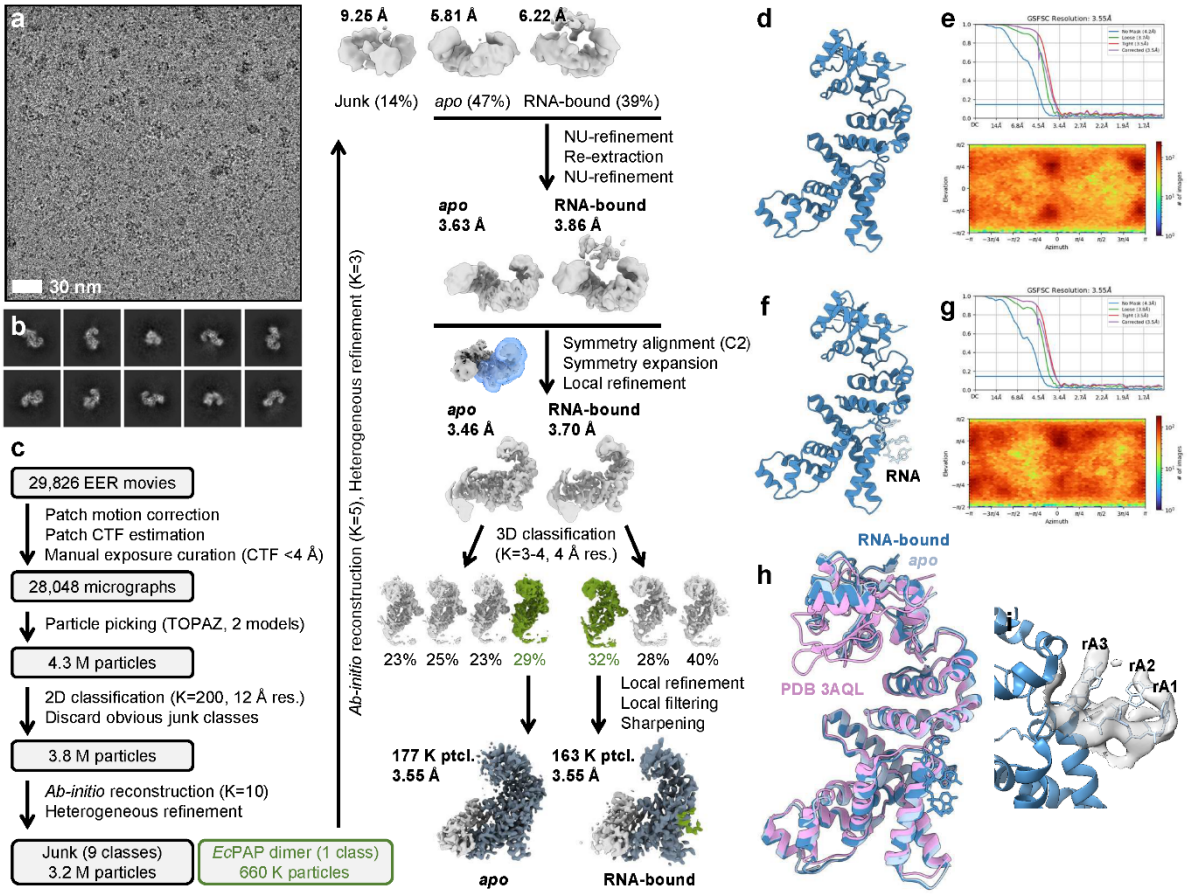

Supplementary Fig. 8 | Cryo-EM data collection, processing, validation, and structural analysis for *apo* and RNA-bound *Ec*PAP

a, Representative motion-corrected, dose-weighted micrograph of mixed *apo* and RNA-bound *Ec*PAP at 165,000x magnification (average defocus 2.14 µm, 5 Å low-pass filtered for clarity). **b,** Representative 2D class averages of mixed *apo* and RNA-bound *Ec*PAP. **c,** Data processing scheme for *apo* and RNA-bound *Ec*PAP. **d-g,** Final atomic model and cryo-EM validation statistics (Fourier shell correlation and orientation distribution) for *apo* **(d-e)** and RNA-bound **(f-g)** *Ec*PAP (asymmetric units, focused refinements). **h,** Structural alignment of *apo* (light blue) and RNA-bound (dark blue) *Ec*PAP cryo-EM structures and a crystal structure of *apo Ec*PAP (PDB 3AQL, pink). **i,** Close-up view of experimental density for peripherally bound RNA in the RNA-bound *Ec*PAP cryo-EM structure (contoured at level 0.10).

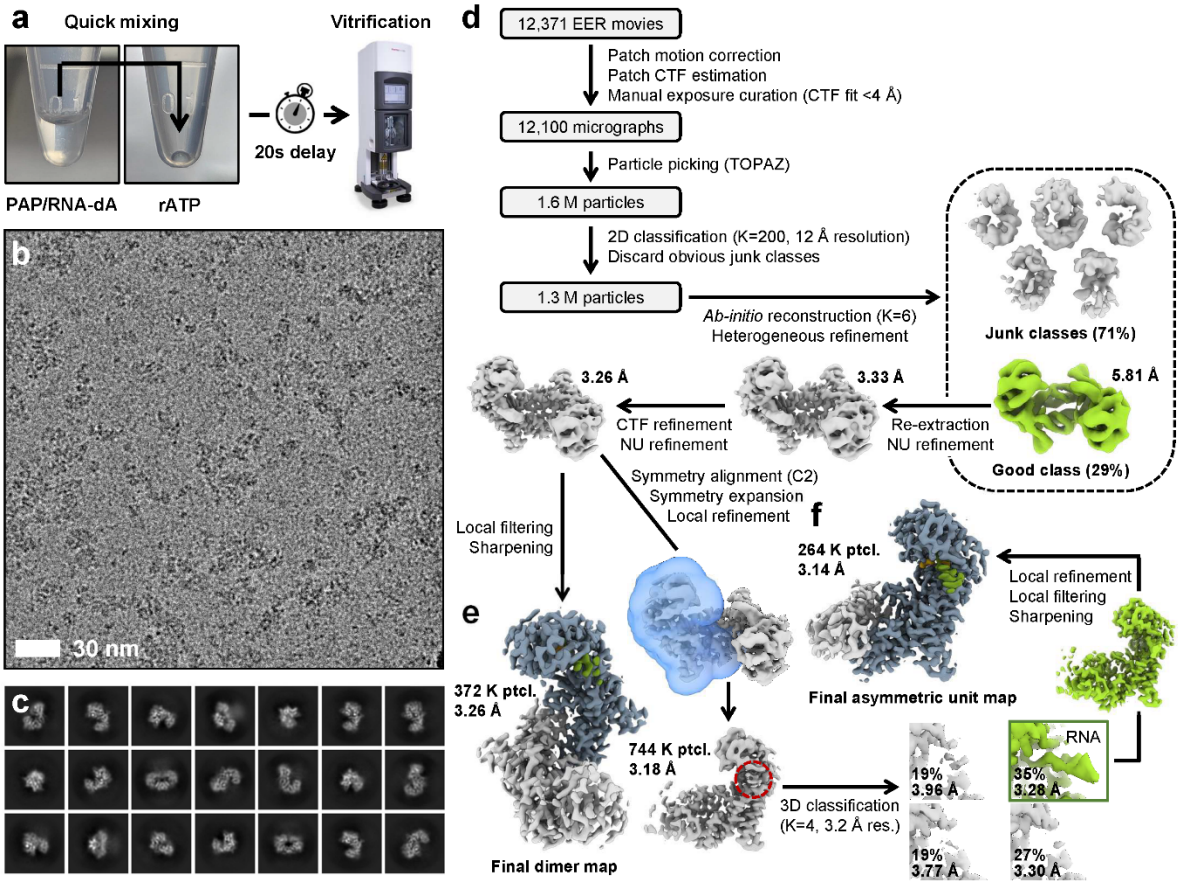

Supplementary Fig. 9 | Cryo-EM data collection and processing for *Ec*PAP:(rA)$_{24}$-dA:rATP complex

a, Brief depiction of workflow used to prepare cryo-EM grids for stalled ternary *Ec*PAP complex. A premix consisting of 1x EM buffer B, *Ec*PAP, (rA)$_{25}$-dA RNA, and *Aav*LEA1 was incubated for >1 h on ice and mixed with rATP immediately prior to vitrification (~20 s delay between mixing and plunge freezing). The liquid samples shown in the images are the actual samples used for cryo-EM data structure determination. **b,** Representative motion-corrected, dose-weighted micrograph of stalled ternary *Ec*PAP complex at 165,000x magnification (average defocus 2.16 µm, 5 Å low-pass filtered for clarity). **c,** Representative 2D class averages of stalled ternary *Ec*PAP complex. **d,** Data processing scheme for stalled ternary *Ec*PAP complex. **e-f,** Final cryo-EM maps for the stalled ternary *Ec*PAP complex dimer (biological unit) **(e)** and asymmetric unit (monomer, focused refinement) **(f)**.

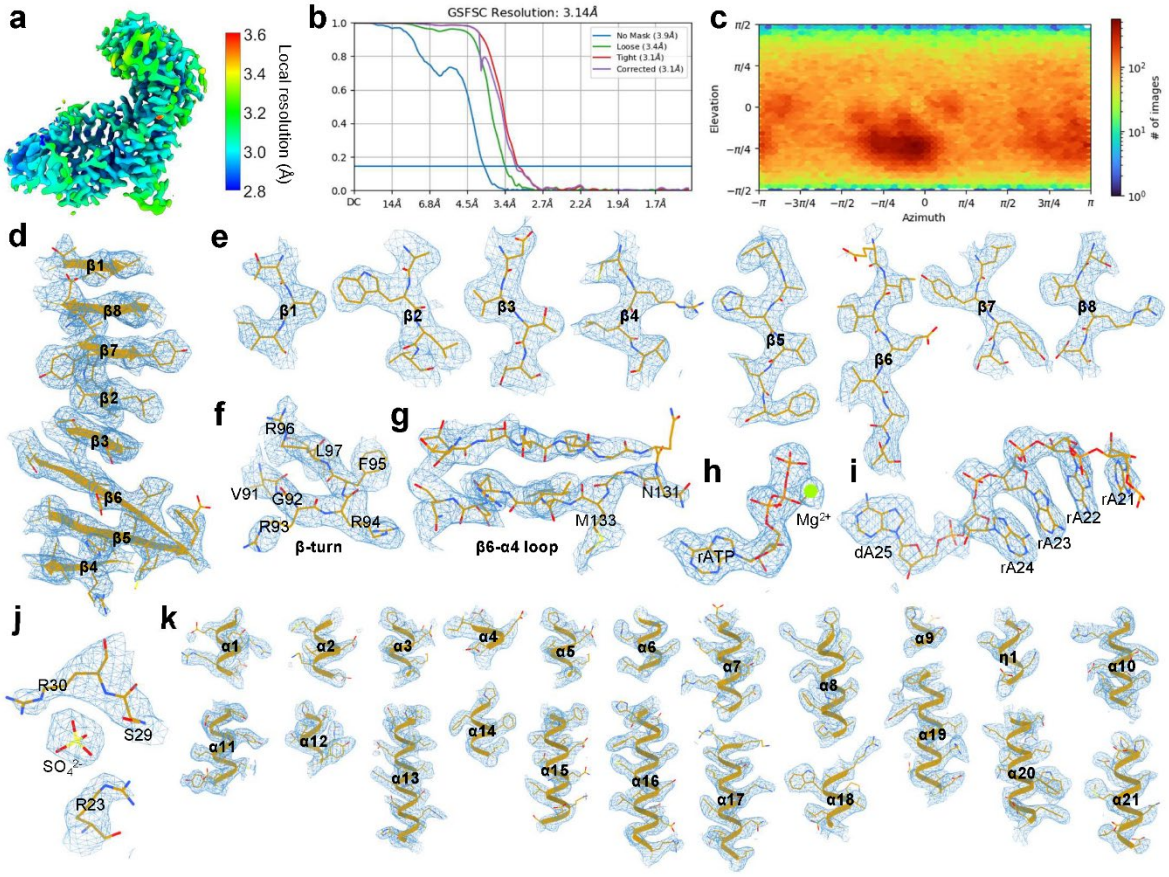

Supplementary Fig. 10 | Cryo-EM data validation and representative density for *Ec*PAP:(rA)$_{24}$-dA:rATP complex (asymmetric unit reconstruction)

a, Local resolution (FSC=0.5) distribution in the ternary *Ec*PAP complex cryo-EM map (asymmetric unit). **b,** Overall Fourier shell correlation (FSC) curves. **c,** Particle orientation distribution plot. **d-k,** Close-up views of key structural elements and corresponding experimental density for the beta sheet β1-8 in the head domain **(d)**, individual beta strands β1-8 **(e)**, the β-turn **(f)**, newly built portion of the β6-α4 loop **(g)**, bound rATP and Mg^{2+} ion **(h)**, resolved segment from bound RNA-dA (rA21-dA25) **(i)**, bound SO_4^{2-} ion and surrounding residues **(j)**, and individual alpha helices α1-α21 and the 3_{10} helix η1 **(k)**.

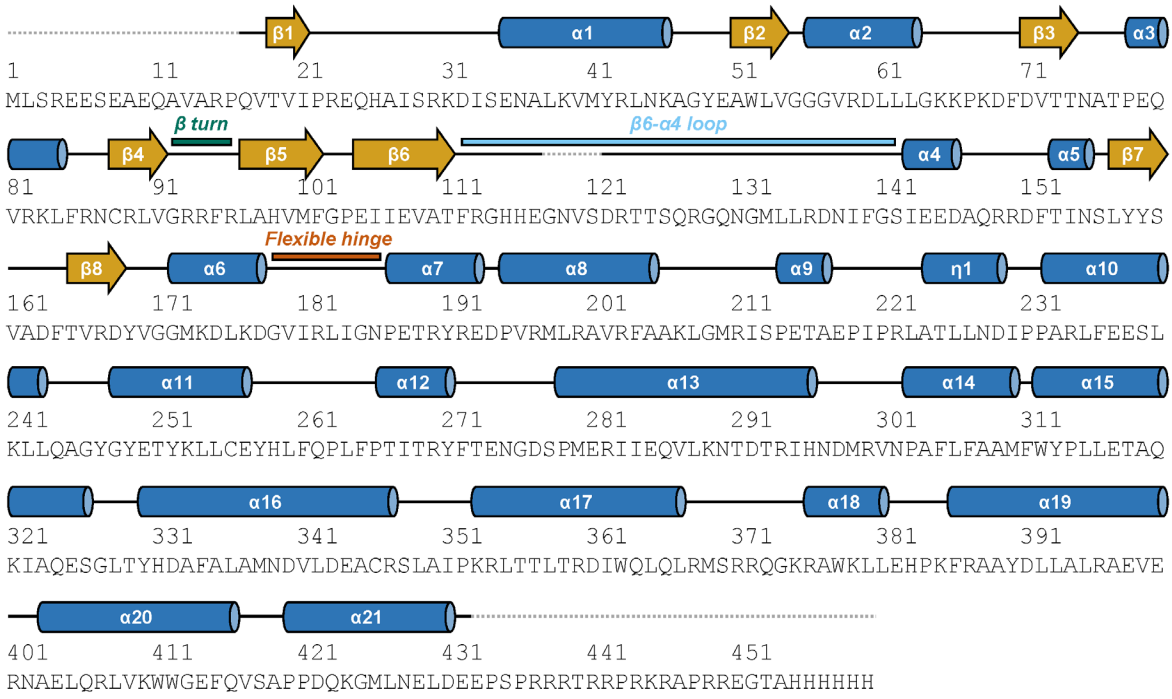

Supplementary Fig. 11 | Experimental secondary structure assignments for *Ec*PAP
The full-length amino acid sequence of the *Ec*PAP construct used for cryo-EM analysis is overlaid with secondary structure assignments derived from the *Ec*PAP:$(rA)_{24}$-dA:rATP complex structure. Both α helices and 3_{10} helices are depicted as blue cylinders, and β strands as orange arrows. For nomenclature, α helices and isolated 3_{10}-helices are numbered with the prefixes α and η, respectively, while β strands are numbered with the prefix β. Transitional 3_{10} helices (<4 amino acids) immediately flanking an α helix are treated as contiguous extensions of that α helix and are not assigned a separate η label. Segments unresolved in the cryo-EM map (M1-P16, G118-S121, and E433-H460) are indicated by gray dotted lines. Key structural motifs (β turn, β6-α4 loop, flexible hinge) are labeled.

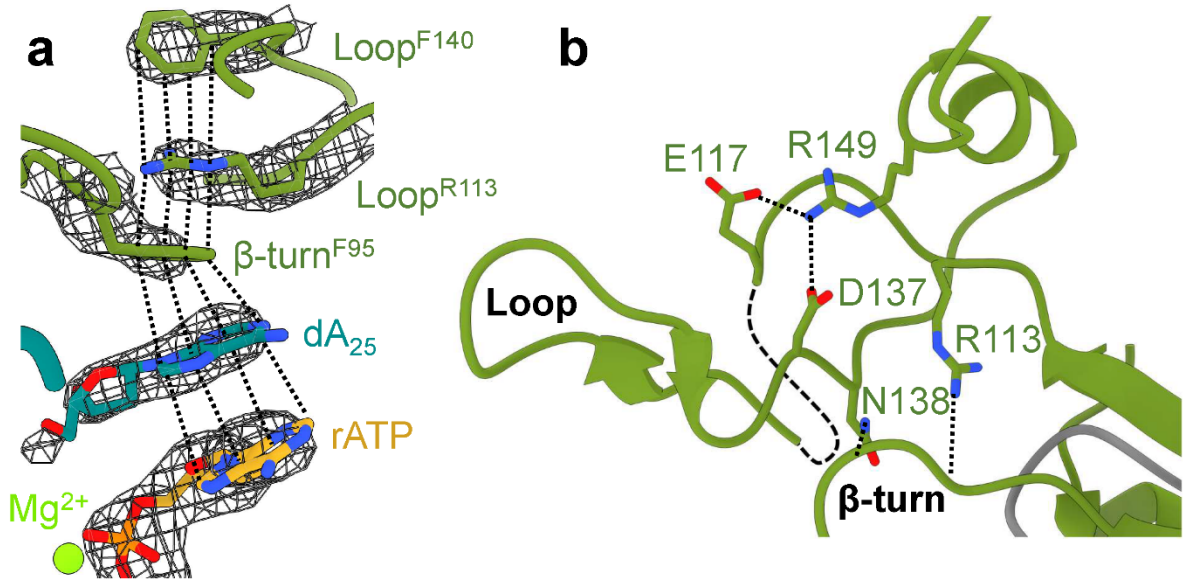

Supplementary Fig. 12 | Detailed interactions involving the β-turn and β6-α4 loop in the ternary *Ec*PAP complex structure

a, A five-way stacking interaction involving the β6-α4 loop residues F140 and R113, β-turn residue F95, primer 3′ terminal nucleobase, and incoming nucleobase. Note the involvement of the β6-α4 loop in clamping the β-turn into its closed conformation. **b,** Extensive polar interactions between β6-α4 loop and β-turn residues in *Ec*PAP (closed conformation).

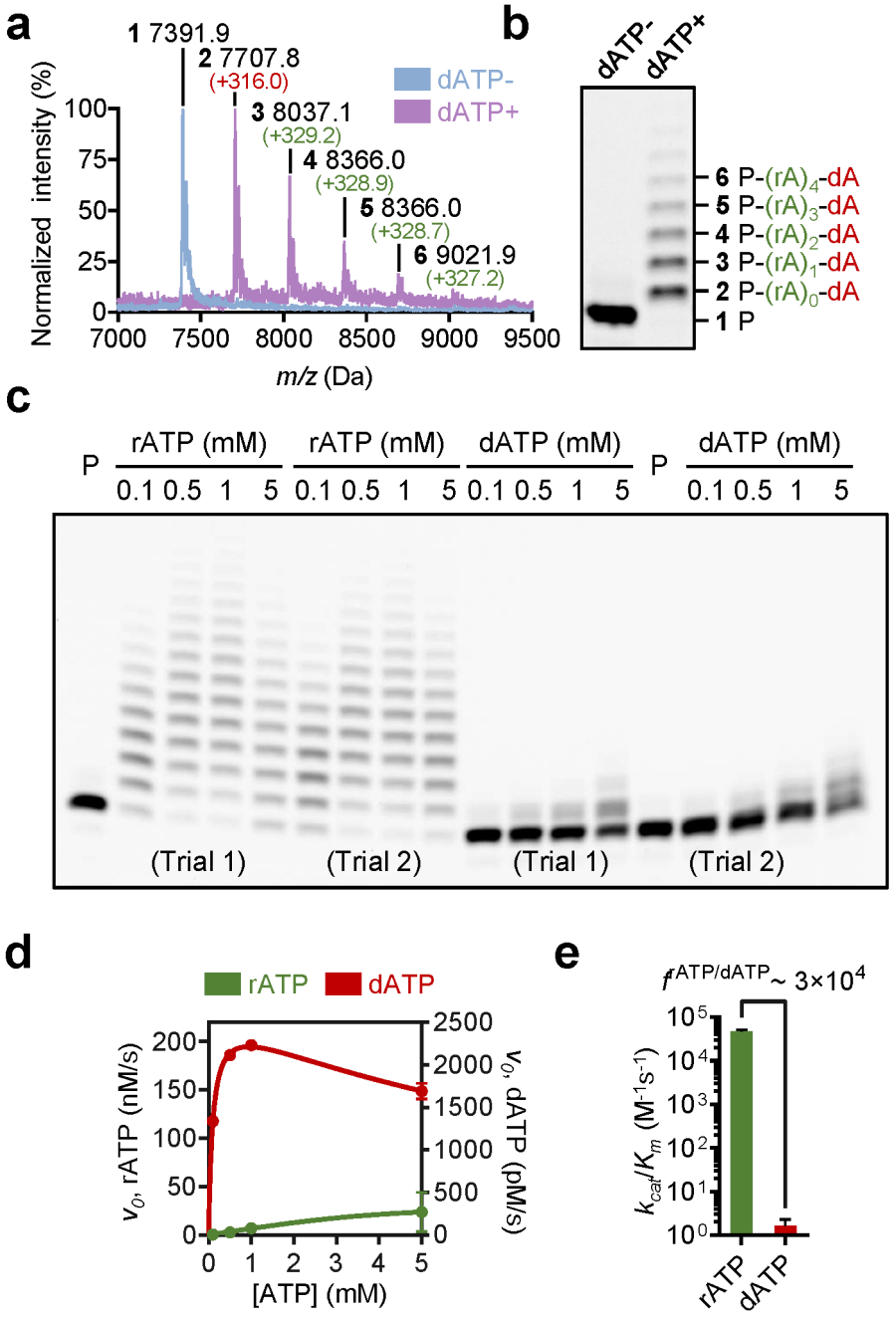

Supplementary Fig. 13 | Practical challenges in realizing *d*MIL using *Ec*PAP
a-b, MALDI-TOF spectrum **(a)** and denaturing PAGE analysis **(b)** of *d*MIL reaction products, synthesized using FAM-$(rA)_{21}$, dATP, and wild-type *Ec*PAP. Cross-identified species are labeled **1-6** in **a** and **b**, with exact chemical composition (*i.e.* P-$(rA)_n$-dA) shown in **b**. Absolute *m*/*z* values and relative differences between adjacent species (in parentheses) are labeled in **a**. **c,** Steady-state primer extension reactions using FAM-$(rA)_{21}$ (denoted "P"), one of rATP or dATP, and wild-type *Ec*PAP. Results for both of the duplicate runs are shown. **d,** Initial velocity data for steady-state primer extension of FAM-$(rA)_{21}$ using either rATP and dATP, calculated from **c**. **e,** Calculated specificity factors (k_{cat}/K_m) for rATP and dATP.

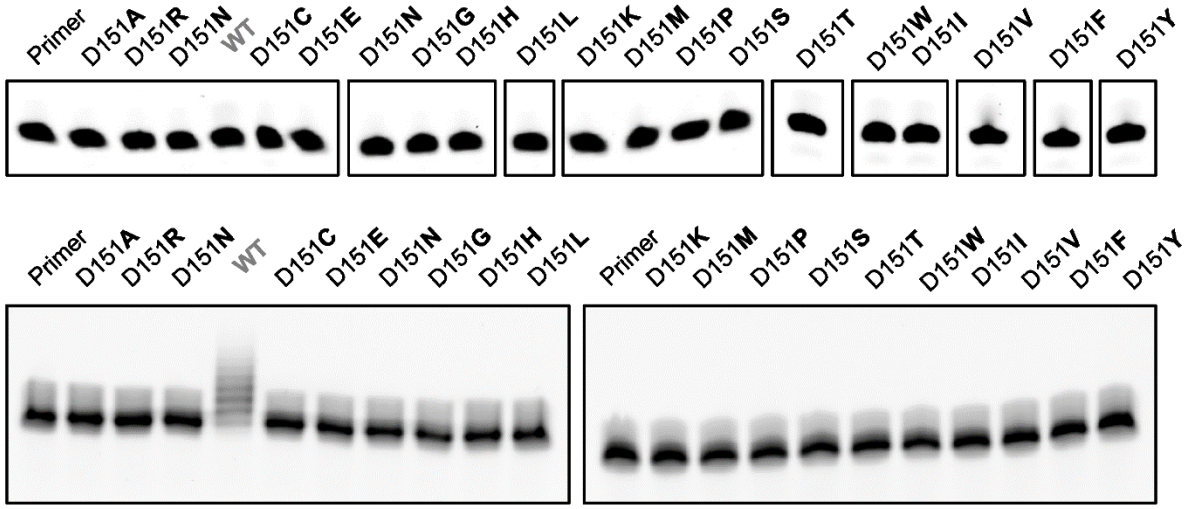

Supplementary Fig. 14 | Site-saturation mutagenesis of *Ec*PAP D151
a, Primer extension of FAM-$(rA)_{21}$ using each *Ec*PAP D151X (site saturation) mutant with dATP. **b,** Primer extension of FAM-$(rA)_{21}$ using each *Ec*PAP D151X (site saturation) mutant with rATP. Reaction products in **a-b** were resolved on 20 × 20 cm 15% Urea-PAGE gels.

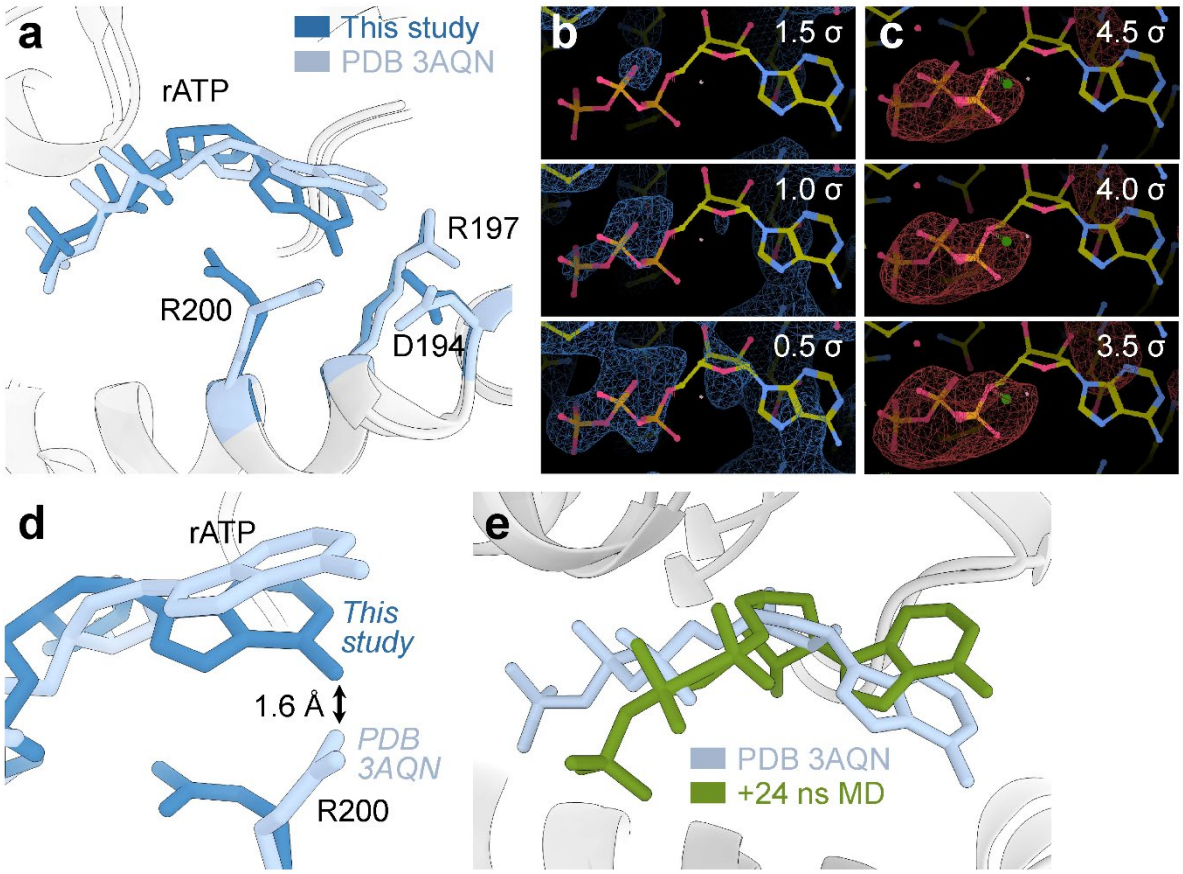

Supplementary Fig. 15 | Deviations in pose for bound rATP between our ternary complex structure and PDB 3AQN

a, Structural alignment between our stalled ternary complex structure (dark blue) and PDB 3AQN (light blue) showing significant deviations in rATP adenine, D194, and R200. **b-c,** Visual inspection of published coordinates and structure factors for PDB 3AQN (chain B) at various map thresholds. $2F_o$-F_c map at 0.5-1.5 σ contour level **(b)** and F_o-F_c (omit) map at 3.5-4.5 σ contour level. Lack of experimental evidence for annotated rATP pose is evident in both **b** and **c**. **d,** The pose for R200 PDB 3AQN is incompatible (due to steric clash) with the rATP adenine pose found in our stalled ternary complex structure. **e,** Pose for bound rATP in PDB 3AQN before (light blue) and after (light green) a 24 ns all-atom molecular dynamics (MD) simulation of the complex (run as per standard protocol in GROMACS 2024 as described in **Methods**). rATP readily dissociates from the published pose in PDB 3AQN.

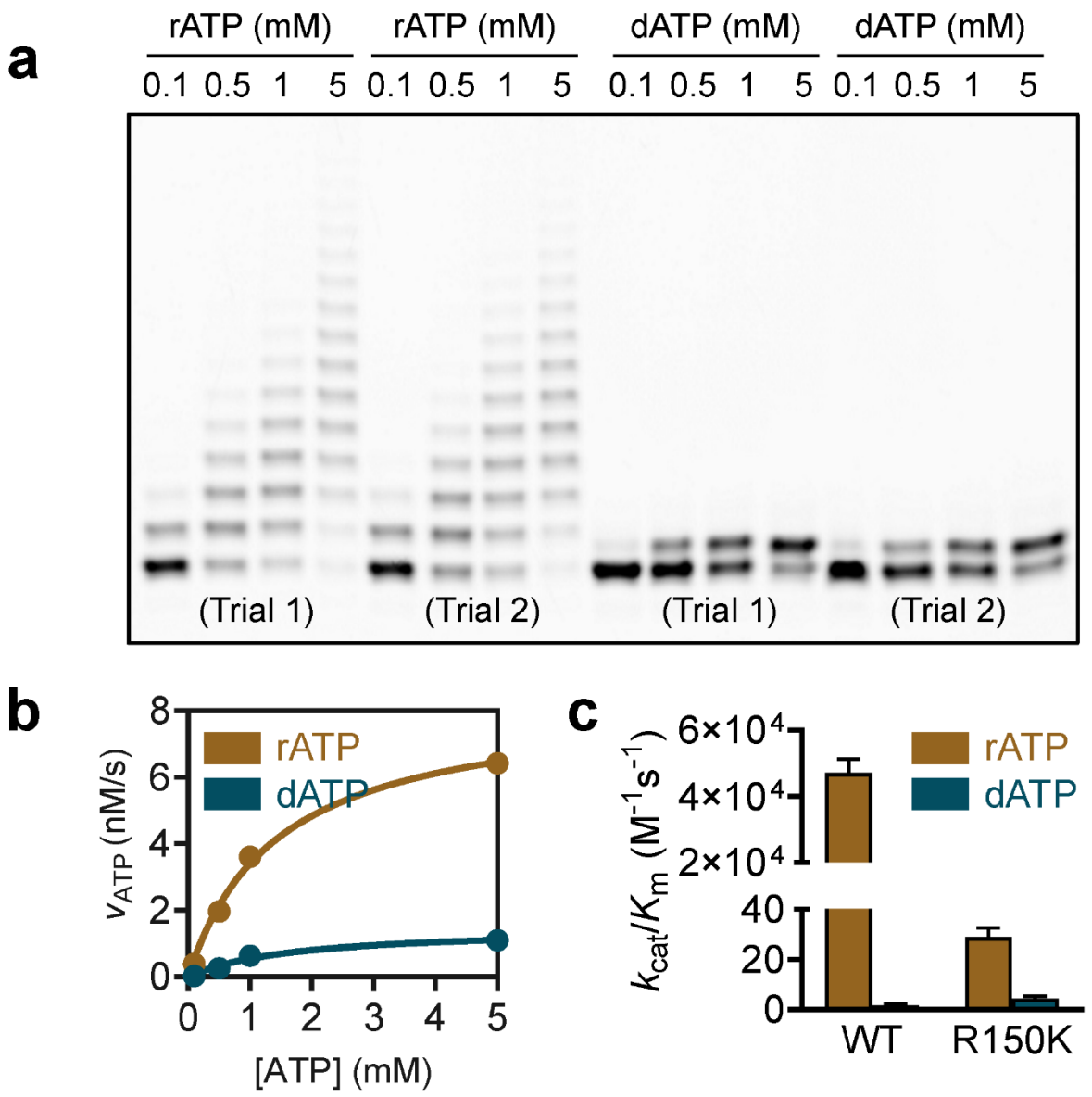

Supplementary Fig. 16 | Steady-state analysis of *Ec*PAP^{R150K} ATP incorporation kinetics **a,** Steady-state primer extension reactions using FAM-$(rA)_{21}$, one of rATP or dATP, and *Ec*PAP^{R150K}. Results for both of the duplicate runs are shown. **b,** Initial velocity data for steady-state primer extension of FAM-$(rA)_{21}$ using either rATP or dATP, calculated from **a**. **c,** Calculated specificity factors (k_{cat}/K_m) for rATP and dATP. Data for wild-type *Ec*PAP ("WT") are from **Supplementary Fig. 13c-e**.

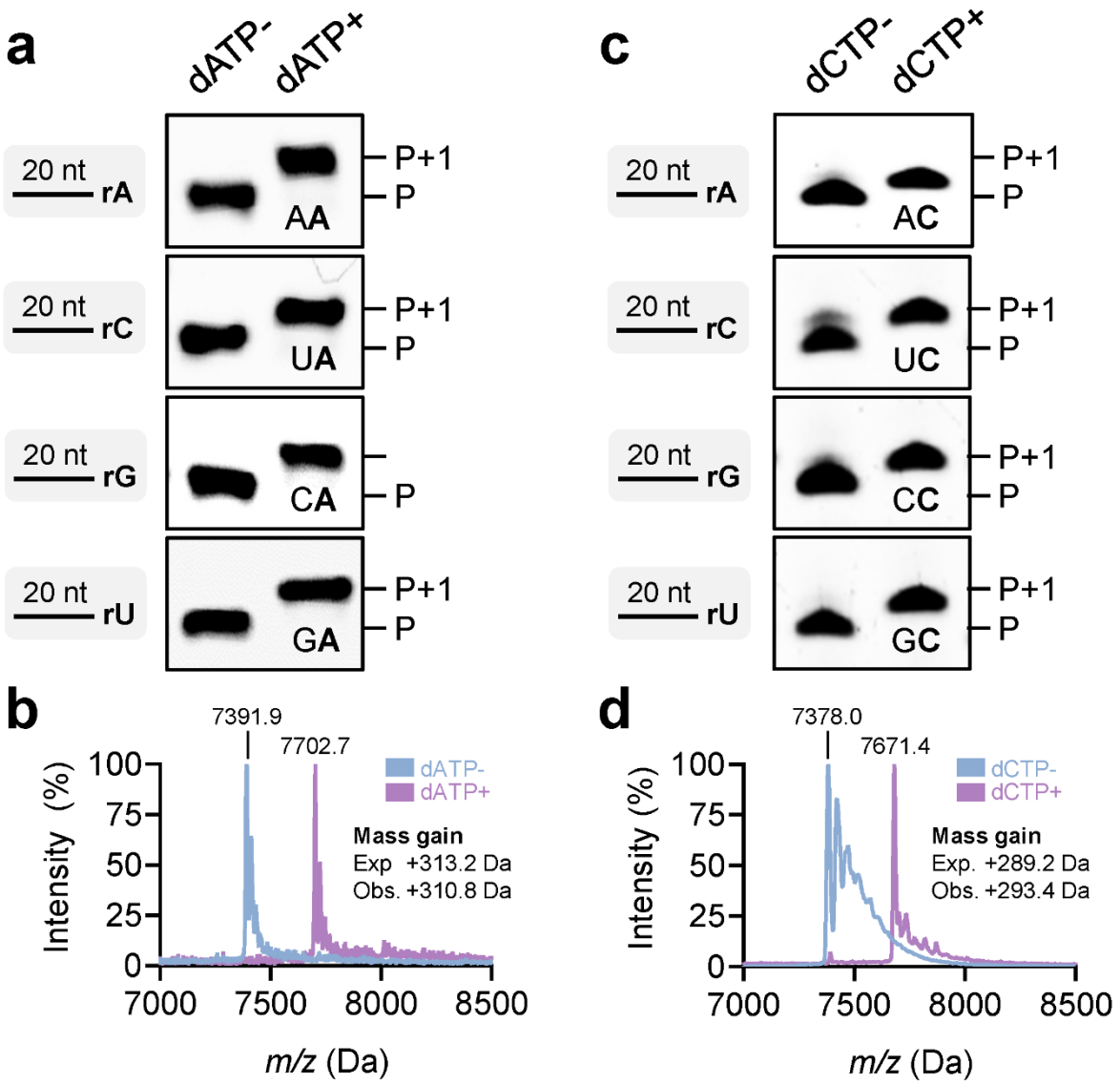

Supplementary Fig. 17 | *Ec*PAP^{R150K} achieves dATP, dCTP *d*MIL with minimal dependence on RNA primer sequence

a, *Ec*PAP^{R150K}-catalyzed *d*MIL reactions with a representative set of RNA oligonucleotides, FAM-$(rA)_{20}$-rN (N=A, C, G, U), and dATP. **b,** MALDI-TOF mass spectra for FAM-$(rA)_{21}$ and its silica column-purified *d*MIL reaction product with dATP. This set corresponds to the topmost row in **a**. **c,** *Ec*PAP^{R150K}-catalyzed *d*MIL reactions with a representative set of RNA oligonucleotides, FAM-$(rA)_{20}$-rN (N=A, C, G, U), and dCTP. **d,** MALDI-TOF mass spectra for FAM-$(rA)_{21}$ and its silica column-purified *d*MIL reaction product with dCTP. This set corresponds to the topmost row in **c**. Expected and observed changes in mass (*m*/*z*) for each *d*MIL reaction are denoted in **b, d**.

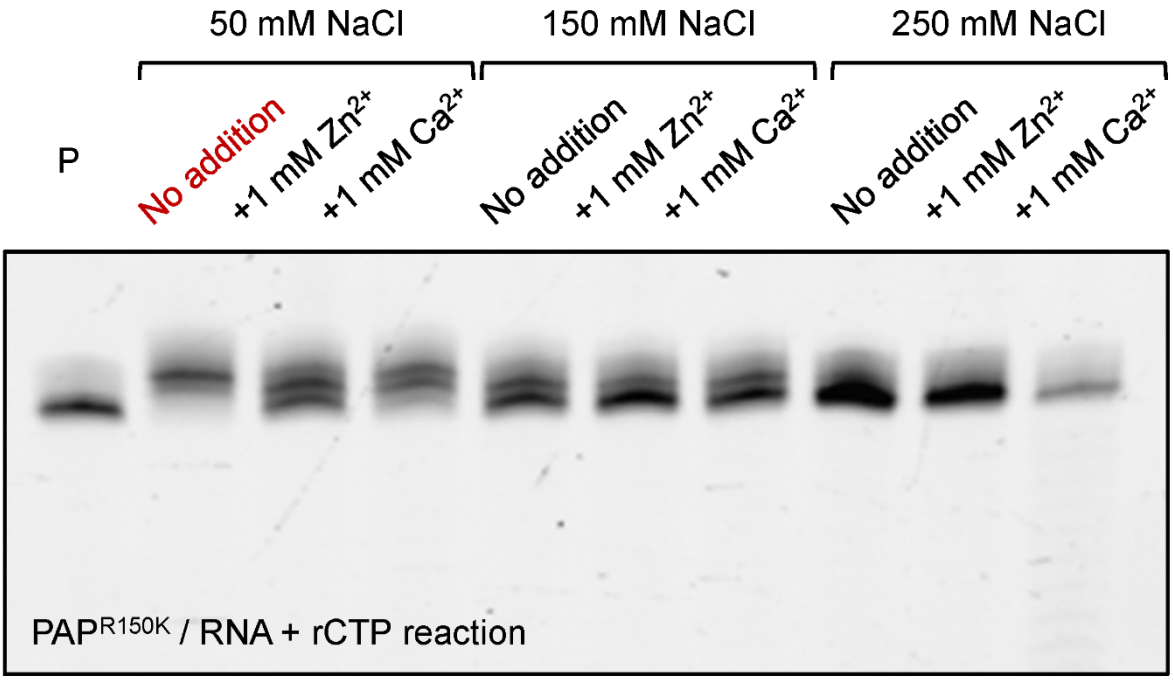

Supplementary Fig. 18 | *Ec*PAP^{R150K} accepts rCTP as substrate under low-salt conditions

*Ec*PAP^{R150K} (1 μM) was incubated with FAM-$(rA)_{21}$ RNA (1 μM) and rCTP (1 mM) under low (50 mM NaCl), medium (150 mM NaCl), or high (250 mM NaCl) salt conditions with or without divalent metal additives ($ZnSO_4$, $CaCl_2$). Note that 10 mM $MgCl_2$ was included in all reactions to be used as the primary divalent metal cofactor. Reactions were carried out at 37 °C for 1 h, quenched using 2x SNL buffer, and analyzed on a 12 × 10 cm 15% TBE/Urea-PAGE gel. Low-salt conditions (regardless of divalent metal additives) are seen to promote incorporation of rCTP by *Ec*PAP^{R150K}.

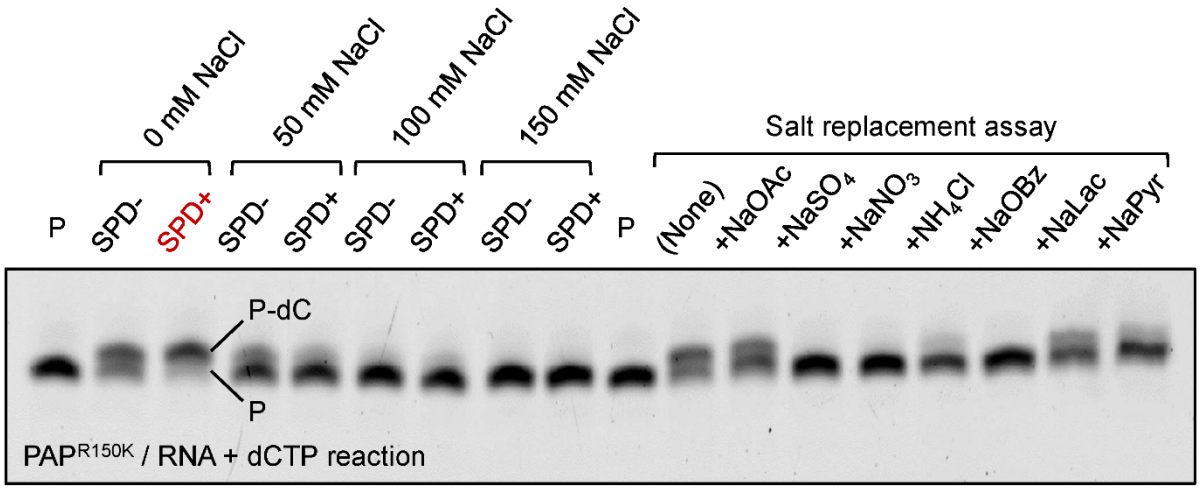

Supplementary Fig. 19 | Additive screening for enhancing dCTP incorporation activity in *Ec*PAP^{R150K}

*Ec*PAP^{R150K} (1 μM) was incubated with FAM-$(rA)_{21}$ RNA (1 μM) and dCTP (1 mM) with various additives (NaCl, SPD, etc.) at 37 °C for 3 h, quenched using 2x SNL buffer, and reaction products analyzed on a 20 × 20 cm 15% TBE/Urea-PAGE gel. Low-salt conditions combined with SPD addition is seen to enable efficient dCTP incorporation by *Ec*PAP^{R150K}.

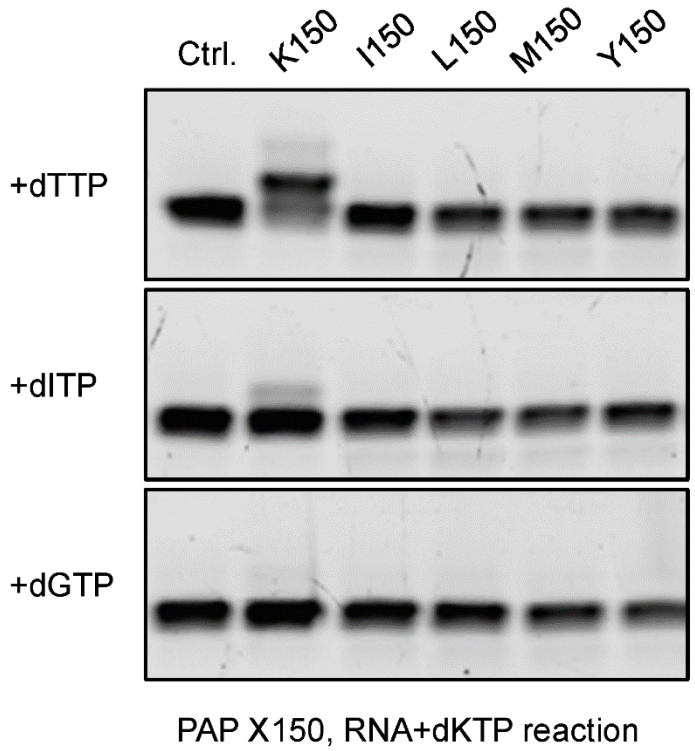

Supplementary Fig. 20 | Incorporation activities of *Ec*PAP R150X mutants towards 3-keto dNTPs

Each *Ec*PAP^{R150X} (X=K, I, L, M, Y) mutant (1 μM) was incubated with FAM-$(rA)_{21}$ RNA (0.5 μM) and one of dTTP, dITP, and dGTP (1 mM) under low-salt conditions (0 mM NaCl) at 37 °C for 5 h, quenched using 2x SNL buffer, and reaction products analyzed on a 20 × 20 cm 15% TBE/Urea-PAGE gel.

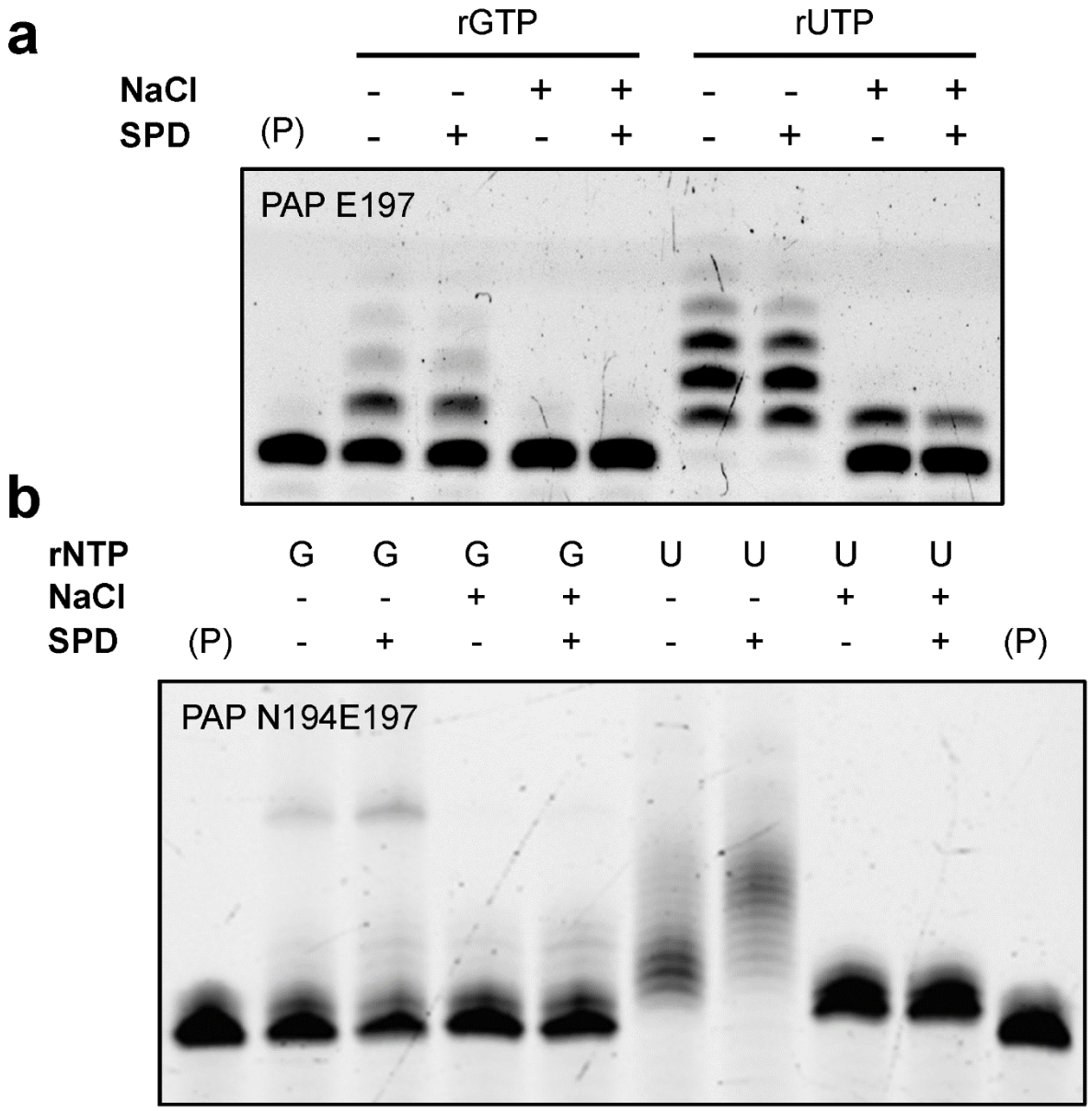

Supplementary Fig. 21 | Incorporation of rGTP, rUTP by hydrogen bond-inverting protein template mutants of *Ec*PAP

Each hydrogen bond-inverting protein template *Ec*PAP mutant (*Ec*PAP^{R197E} **(a)**, *Ec*PAP$^{D194N/R197E}$ **(b)**) (1 µM) was incubated with FAM-$(rA)_{21}$ RNA (0.5 µM) and one of rGTP and rUTP under low-salt ("NaCl-", 0 mM NaCl) or high-salt ("NaCl+", 200 mM NaCl) conditions with or without 5 mM SPD at 37 °C for 5 h. Reactions were quenched using 2x SNL buffer and reaction products analyzed on a 12 × 10 cm **(a)** or 20 × 20 cm **(b)** 15% TBE/Urea-PAGE gel. Both hydrogen bond-inverting mutations are seen to enable incorporation of rGTP and rUTP when introduced to wild-type *Ec*PAP.

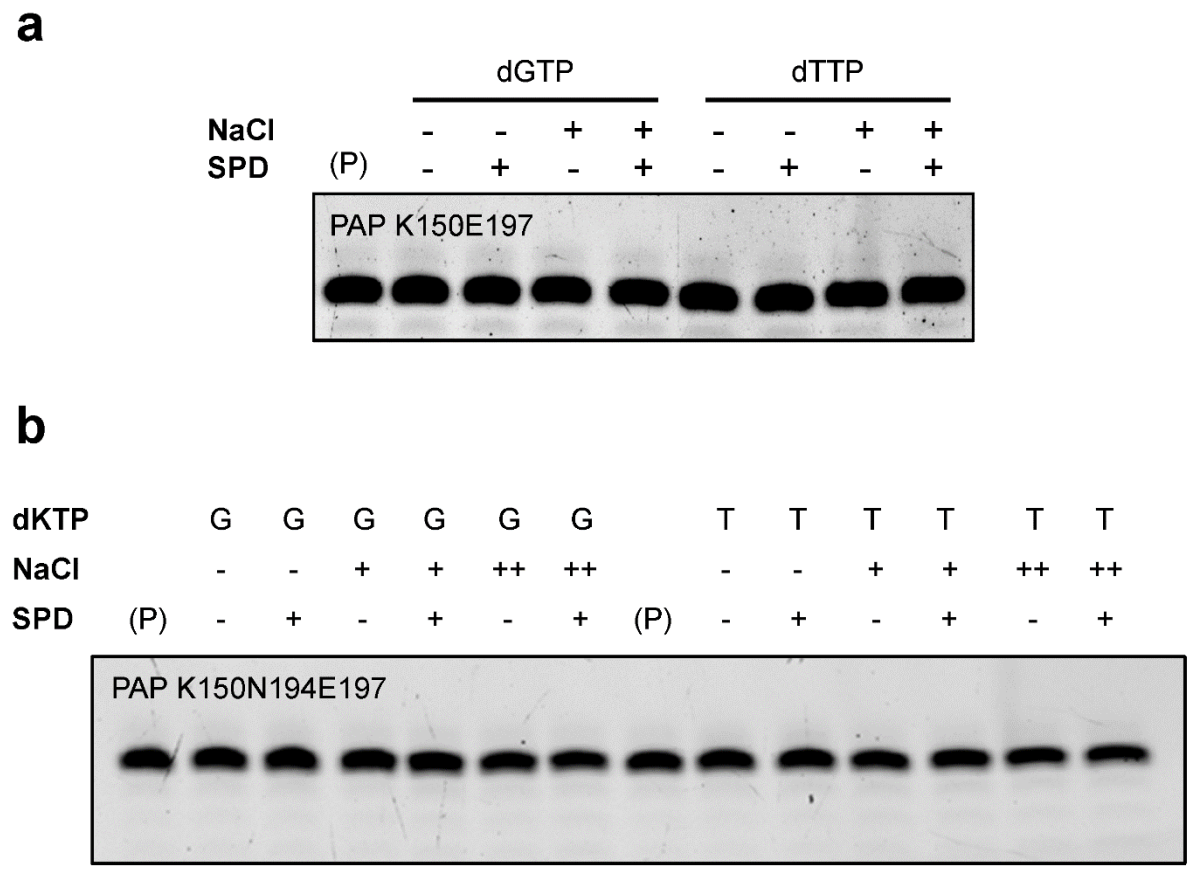

Supplementary Fig. 22 | Incorporation of dGTP, dTTP by hydrogen bond-inverting protein template mutants of *Ec*PAP^{R150K}

Each hydrogen bond-inverting protein template *Ec*PAP^{R150K} mutant (*Ec*PAP$^{R150K/R197E}$ **(a)**, *Ec*PAP$^{R150K/D194N/R197E}$ **(b)**) (1 µM) was incubated with FAM-$(rA)_{21}$ RNA (0.5 µM) and one of dGTP and dTTP with or without 5 mM SPD at 37 °C for 5 h. In **a,** "NaCl-" and "NaCl+" refer to reactions with 0, 200 mM NaCl, respectively. In **b**, "NaCl-", "NaCl+", and "NaCl++" refer to reactions with 0, 50, and 150 mM NaCl, respectively. Reactions were quenched using 2x SNL buffer and reaction products analyzed on 20 × 20 cm 15% TBE/Urea-PAGE gels. Both hydrogen-bond inverting mutations lead to loss of activity when introduced to *Ec*PAP^{R150K}.

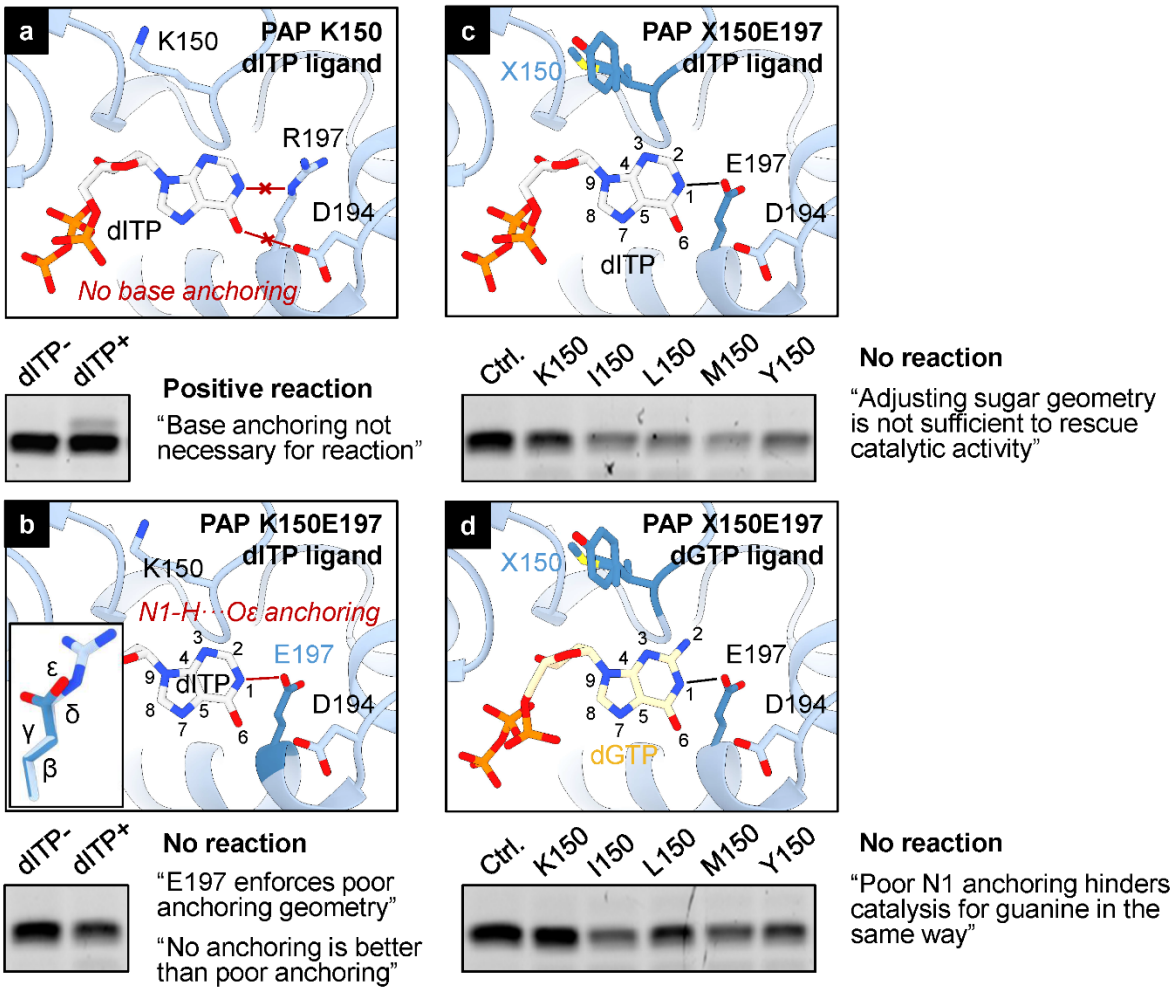

Supplementary Fig. 23 | Combining R197E with alternative R150 mutations fails to rescue *Ec*PAP activity

All primer extension reactions were carried out with purified *Ec*PAP mutant (1 µM), FAM-$(rA)_{21}$ RNA (0.5 µM), and one of dGTP and dITP (1 mM) under low-salt (0 mM NaCl) conditions at 37 °C for 5 h. Reactions were quenched using 2x SNL buffer and reaction products analyzed on 20 × 20 cm 15% TBE/Urea-PAGE gels. **a,** The base mutant *Ec*PAP^{R150K} shows marginal activity towards dITP, showing that Watson-Crick hydrogen bonds between the protein template residues (D194, R197) and incoming nucleobase are not an absolute requirement for activity. **b,** Combining the sugar binding pocket mutation R150K with the protein template mutation R197E, meant to form a productive hydrogen bond with the 1-NH edge of guanine or hypoxanthine, leads to loss of activity towards dITP. This shows that E197 anchors dITP in a suboptimal conformation and no anchoring (as in **a**, where marginal activity was present towards dITP) is better than poor anchoring in the context of the *Ec*PAP protein template. **c,** Combining the R197E mutation with alternative sugar binding pocket mutations (R150X, X=K, I, L, M, Y) fails to rescue activity. This shows that adjusting sugar binding geometry is not sufficient to rescue activity towards dITP upon anchoring via E197. **d,** The same results as in **c** could be replicated for dGTP as well, showing that poor 1-NH anchoring via E197 hinders catalysis for dGTP as well.

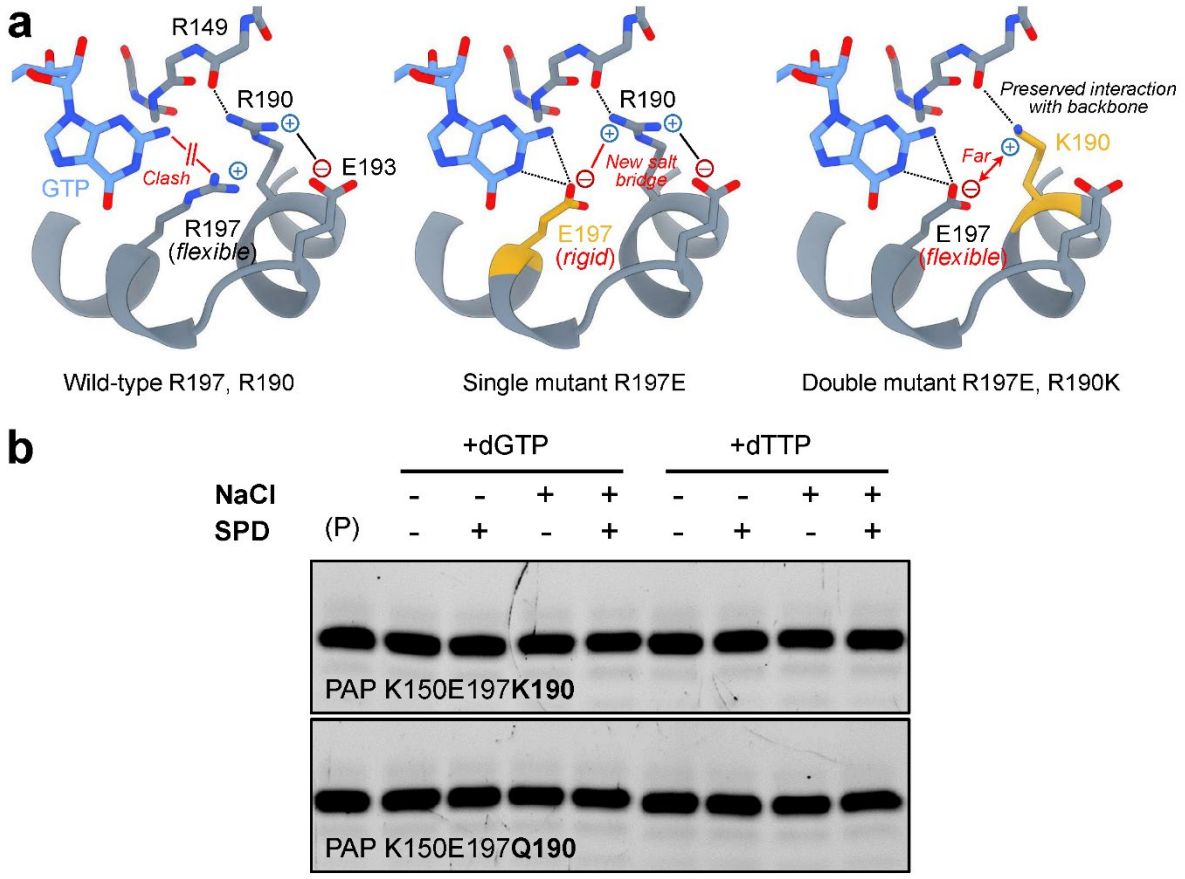

Supplementary Fig. 24 | *De novo* salt E197-R190 salt bridge formation in *Ec*PAP R197E mutants and disruption by R190 mutagenesis

a, Introduction of the hydrogen-bond inverting mutation R197E forms an unintentional salt bridge between E197 and R190 *de novo*, potentially fixing E197 in a nonproductive conformation and leading to loss of catalytic activity. In an effort to rescue activity in *Ec*PAP R197E mutants, we sought to mutate R190 to Lys or Gln in an effort to weaken this salt bridge without disrupting the overall fold of the *Ec*PAP active site. **b,** *Ec*PAP$^{R150K/R190K/R197E}$ and *Ec*PAP$^{R150K/R190Q/R197E}$ (1 μM) were each incubated with FAM-$(rA)_{21}$ RNA (0.5 μM) and one of dGTP and dTTP (1 mM) under low-salt (“NaCl-”, 0 mM NaCl) or high-salt (“NaCl+”, 200 mM NaCl) conditions with or without 5 mM SPD at 37 °C for 6 h. Reactions were quenched using 2x SNL buffer and reaction products analyzed on a 20 × 20 cm TBE/Urea-PAGE gel. R190 mutagenesis is unable to rescue activity in *Ec*PAP R197E mutants.

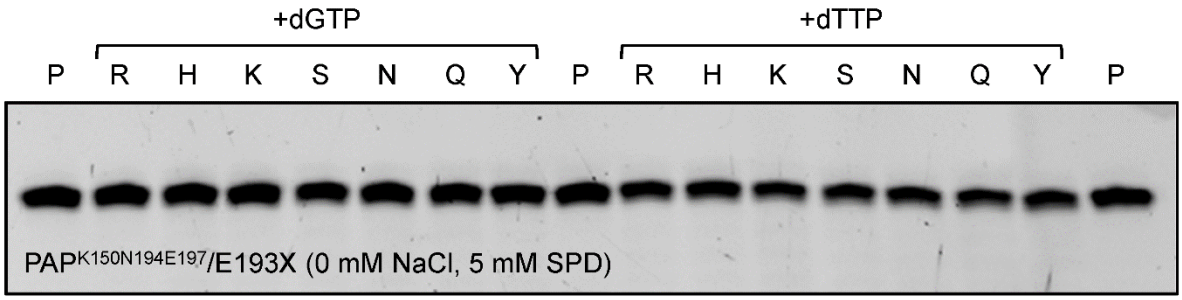

Supplementary Fig. 25 | Mutations in the second-sphere residue E193 fails to rescue activity in *Ec*PAP$^{R150K/D194N/R197E}$

The second-sphere residue E193 (adjacent to R190 as shown in **Supplementary Fig. 24a**) was mutated in an effort rescue activity in *Ec*PAP R197E mutants. Each *Ec*PAP$^{R150K/E193X/D194N/R197E}$ (X=R, H, K, S, N, Q, Y) (1 μM) was incubated with FAM-$(rA)_{21}$ RNA (1 μM) one of dGTP and dTTP (1 mM) under low-salt conditions (0 mM NaCl) with 5 mM SPD at 37 °C for 1 h. Reactions were quenched using 2x SNL buffer and reaction products analyzed on a 20 × 20 cm TBE/Urea-PAGE gel. E193 mutagenesis is unable to rescue activity in *Ec*PAP R197E mutants.

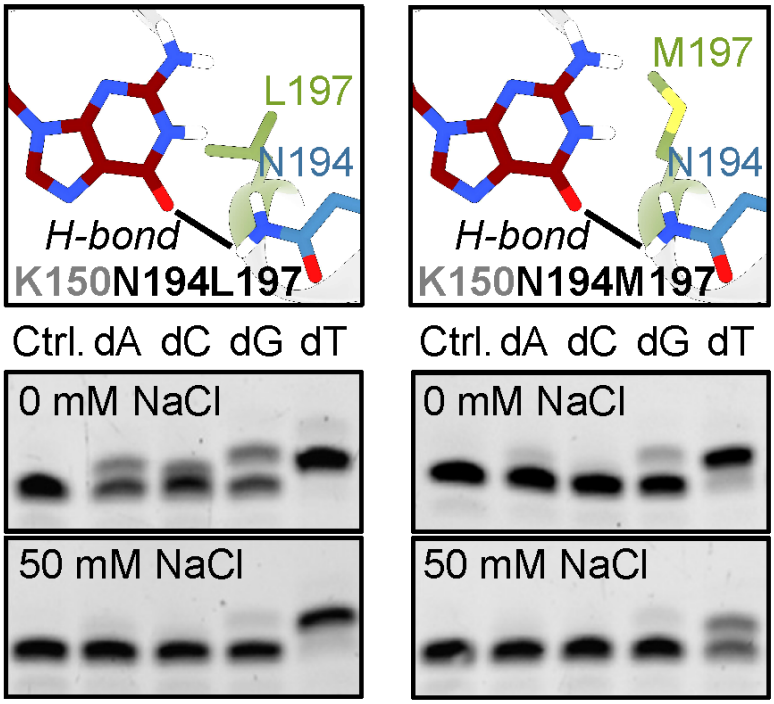

Supplementary Fig. 26 | Nucleobase specificity in *Ec*PAP$^{R150K/D194N/R197X}$ (X=L, M) mutants Primer extension of FAM-$(rA)_{21}$ using *Ec*PAP$^{R150K/D194N/R197L}$ or *Ec*PAP$^{R150K/D194N/R197M}$ with either one of the four canonical dNTPs (dATP, dCTP, dGTP, dTTP) under low (0 mM), medium (50 mM), or high (150 mM) NaCl concentration. The modeled structure of each *Ec*PAP mutant bound to dGTP is shown above as well.

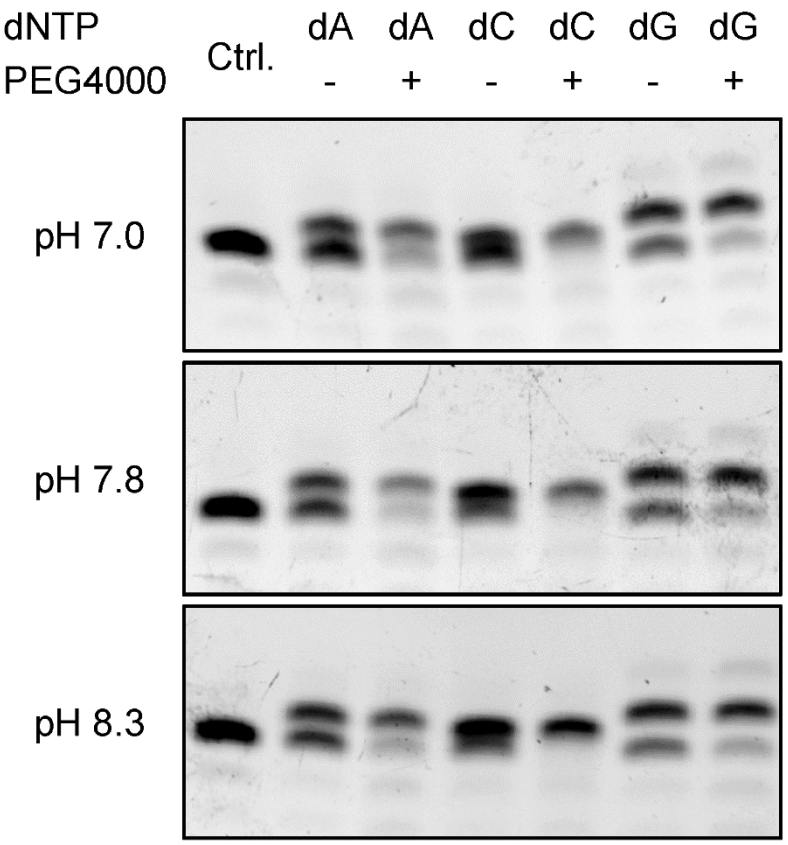

Supplementary Fig. 27 | Effect of solution pH and PEG addition on *d*MIL activity/fidelity in *Ec*PAP$^{R150K/D194N/R197L}$

The effects of solution pH and PEG addition on dNTP incorporation activity and *d*MIL fidelity by *Ec*PAP$^{R150K/D194N/R197L}$ was investigated. *Ec*PAP$^{R150K/D194N/R197L}$ (1 μM) was incubated with FAM-$(rA)_{21}$ RNA (0.5 μM) and one of dATP, dCTP, and dGTP (1 mM) at pH 7.0, 7.8, or 8.3 with or without PEG addition (5 mM SPD included in all reactions) at 37 °C for 6 h. Reactions were quenched using 2x SNL buffer and reaction products analyzed on a 20 × 20 cm TBE/Urea-PAGE gel. PEG is seen to stimulate activity but lead to increased N+2 product formation for dGTP. pH-dependent effects are negligible under the conditions assayed.

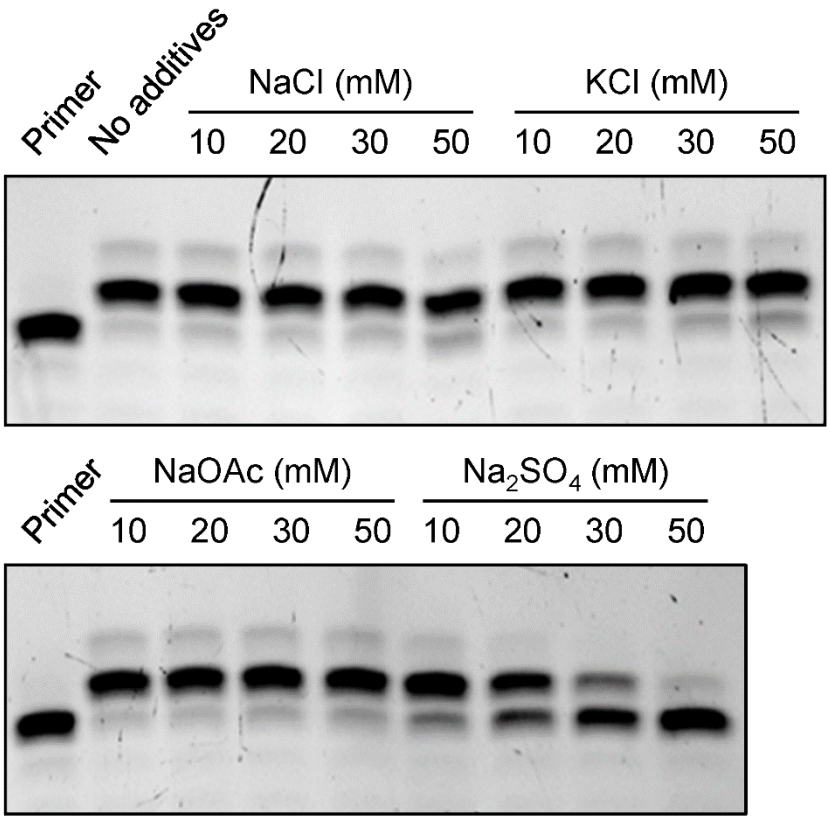

PAP K150N194L197, RNA+dGTP *d*MIL reactions
(50 mM MOPS, 5 mM SPD, 10% PEG4000, 0.2 μM RNA, 2 mM dGTP, 30 ℃)

Supplementary Fig. 28 | Effect of salt additives on *d*MIL activity/fidelity in *Ec*PAP$^{R150K/D194N/R197L}$

The effects of salt additives on dNTP incorporation activity and *d*MIL fidelity by *Ec*PAP$^{R150K/D194N/R197L}$ was investigated. *Ec*PAP$^{R150K/D194N/R197L}$ (1 μM) was incubated with FAM-$(rA)_{21}$ RNA (0.2 μM) and dGTP (2 mM) with or without salt additives (NaCl, KCl, NaOAc, Na_2SO_4) at various concentrations (5 mM SPD, 10% PEG included in all reactions) at 30 °C for 5 h. Reactions were quenched using 2x SNL buffer and reaction products analyzed on a 20 × 20 cm TBE/Urea-PAGE gel. Salt additives are seen to be ineffective in suppressing N+2 product formation.

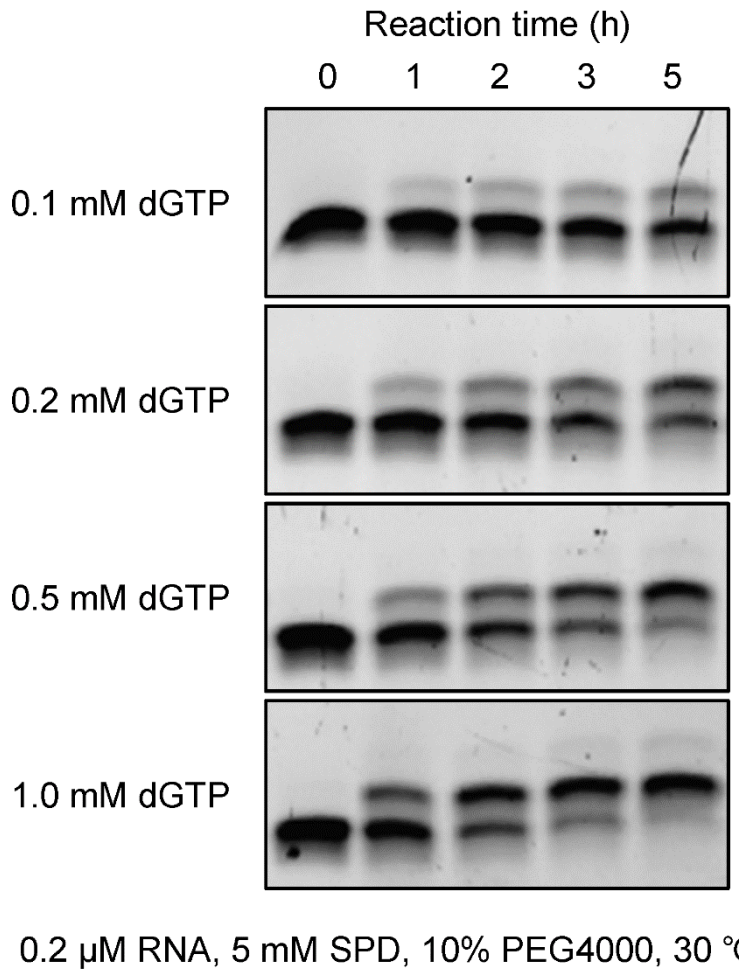

Supplementary Fig. 29 | Effect of dGTP concentration and reaction time on *d*MIL fidelity in *Ec*PAP$^{R150K/D194N/R197L}$

*Ec*PAP$^{R150K/D194N/R197L}$ (1 μM) was incubated with FAM-$(rA)_{21}$ RNA (0.2 μM) and dGTP at various concentrations (0.1-1 mM) (5 mM SPD, 10% PEG included in all reactions) at 30 °C. Samples were drawn from each reaction after 1, 2, 3, and 5 h to analyze the fidelity of *d*MIL as a function of both dGTP concentration and reaction time. Reactions were quenched using 2x SNL buffer and reaction products analyzed on a 20 × 20 cm TBE/Urea-PAGE gel. The N+2 extension product is seen to accumulate before N→N+1 (intended *d*MIL reaction) extension is complete regardless of dGTP concentration.

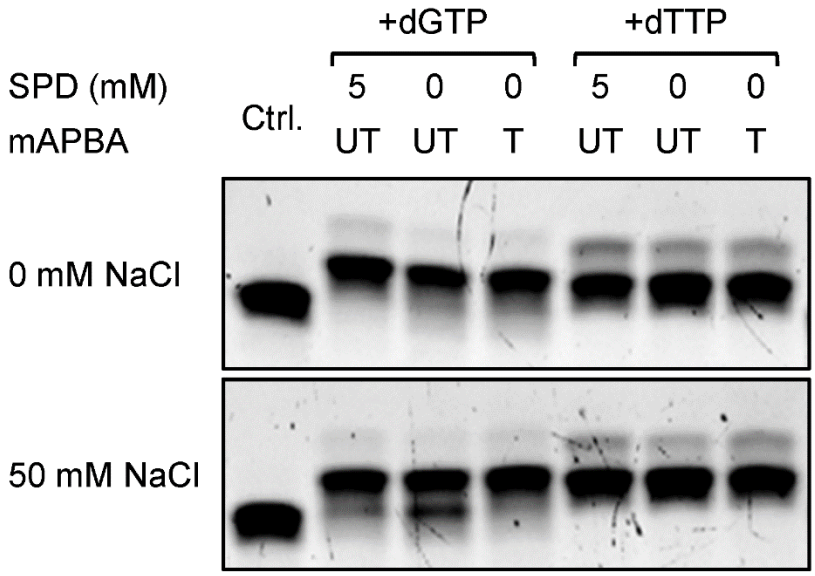

UT = Untreated, T = Treated
0.2 μM RNA, 2 mM dNTP, 10% PEG4000, 30 ℃ (6 h rxn)

Supplementary Fig. 30 | Effect of *m*-aminophenylboronate agarose (*m*APBA) resin treatment and NaCl concentration on *d*MIL fidelity in *Ec*PAP$^{R150K/D194N/R197L}$
To exclude ribonucleotide contamination as a cause for N+2 product formation in *Ec*PAP$^{R150K/D194N/R197L}$-catalyzed *d*MIL reactions, we passed the dGTP, dTTP stock solutions through an *m*APBA resin (known to bind specifically to ribonucleotides but exclude deoxyribonucleotides) prior to reaction. *Ec*PAP$^{R150K/D194N/R197L}$ (1 μM) was incubated with FAM-$(rA)_{21}$ RNA (0.2 μM) and one of dGTP and dTTP (either mAPBA-untreated, "UT" or mAPBA-treated "T") (2 mM) under low-salt (0 mM NaCl) or medium-salt (50 mM NaCl) conditions with or without 5 mM SPD addition (10% PEG included in all reactions) at 30 °C for 6 h. Reactions were quenched using 2x SNL buffer and reaction products analyzed on a 20 × 20 cm TBE/Urea-PAGE gel. *m*APBA resin treatment is seen to be ineffective in suppressing N+2 product formation, excluding ribonucleotide contamination as a cause for loss of *d*MIL fidelity.

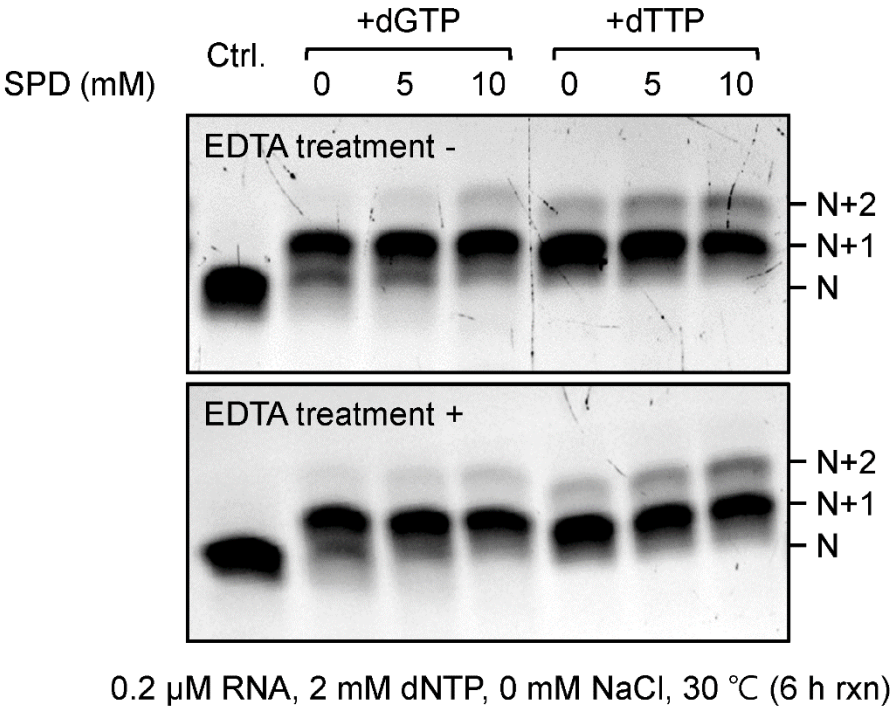

Supplementary Fig. 31 | Effect of EDTA pre-treatment and spermidine concentration on *d*MIL fidelity in *Ec*PAP$^{R150K/D194N/R197L}$

To exclude Co^{2+} contamination (from the TALON resin used for purification) as a cause for N+2 product formation in *Ec*PAP$^{R150K/D194N/R197L}$-catalyzed *d*MIL reactions, we pre-incubated the *Ec*PAP$^{R150K/D194N/R197L}$ stock solution with 1 mM EDTA for 5 min on ice prior to reaction. Note that the binding affinity of EDTA-Co^{2+} is several orders of magnitude stronger than that of EDTA-Mg^{2+}, preventing the Mg^{2+} in the reaction buffer from displacing Co^{2+} from its EDTA-bound state. *Ec*PAP$^{R150K/D194N/R197L}$ (either EDTA pre-treated or untreated) (1 μM) was incubated with FAM-$(rA)_{21}$ RNA (0.2 μM) and one of dGTP and dTTP (2 mM) under low-salt (0 mM NaCl) conditions with 0-10 mM SPD and 10% PEG at 30 °C for 6 h. Reactions were quenched using 2x SNL buffer and reaction products analyzed on a 20 × 20 cm TBE/Urea-PAGE gel. EDTA pre-treatment is seen to be ineffective in suppressing N+2 product formation, excluding Co^{2+} contamination as a cause for loss of *d*MIL fidelity.

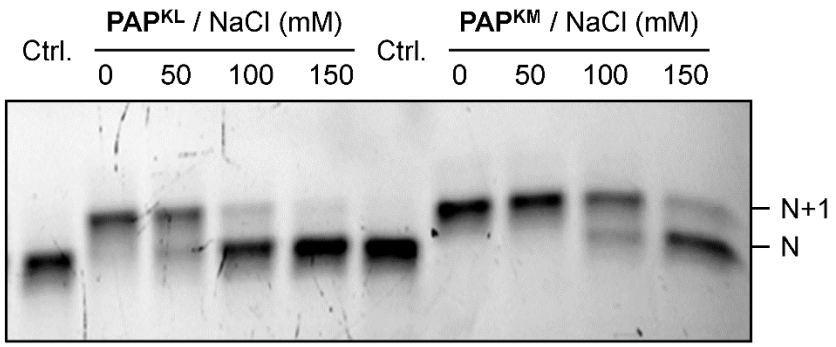

0.2 μM RNA, 2 mM dGTP, 10% PEG4000, 10 mM SPD, 1 M betaine, 30 ℃ (6 h rxn)

Supplementary Fig. 32 | Effect of betaine addition on dGTP *d*MIL activity in *Ec*PAP$^{R150K/R197X}$ (X=L, M) mutants

Each *Ec*PAP$^{R150K/R197X}$ (X=L, M) mutant (1 μM) was incubated with FAM-$(rA)_{21}$ RNA (0.2 μM) and dGTP (2 mM) with 0-150 mM NaCl, 10 mM SPD, 10% PEG, and 1 M TMG at 30 °C for 6 h. Reactions were quenched using 2x SNL buffer and reaction products analyzed on a 20 × 20 cm TBE/Urea-PAGE gel.

SUPPLEMENTARY TABLES

Supplementary Table 1. Cryo-EM data collection, refinement and validation statistics

	***Ec*PAP (*apo*, 1mer)** EMD-80252 PDB 25OJ	***Ec*PAP:$(rA)_{24}$-dA:rATP (1mer)** EMD-80253 PDB 25OK	***Ec*PAP:$(rA)_{24}$-dA:rATP (2mer)** EMD-80254 PDB 25OL
Data collection			
Microscope		Titan Krios G4	
Energy filter		Selectris X	
Camera		Falcon 4i	
Acceleration voltage (kV)		300	
Nominal magnification		165,000x	
Calibrated pixel size (Å/px)		0.75	
C2 aperture width (µm)		50	
Illumination area (nm)		600	
Image navigation		AFIS	
Exposures per hole		4	
Total dose ($e^-/Å^2$)		60	
Dose rate ($e^-/Å^2/s$)	16.56	17.02	
Nominal defocus range (µm)	0.5 – 2.5	1.0 – 2.5	
Micrographs collected	29,826	12,371	
Image processing			
Reconstruction software		CryoSPARC v4.3.1	
Initial particle stack	3,934,575	1,602,043	
Final particle stack	177,275	163,082	371,971
Symmetry	C1 (C2 expanded)	C1 (C2 expanded)	C1
Resolution (Å)			
FSC 0.143 (overall)	3.55	3.14	3.26
Model building			
Chains	1	2	4
Atoms	2,929 (hydrogens: 0)	3,560 (hydrogens: 0)	6,883 (Hydrogens: 0)
Residues	Protein: 359 Nucleotide: 0	Protein: 412 Nucleotide: 5	Protein: 813 Nucleotide: 8
Ligands	0	MG: 1, SO4: 1, ATP: 1	MG: 2, SO4: 2, ATP: 2
Bonds (RMSD)			
Length (Å) (# > 4σ)	0.003 (0)	0.003 (0)	0.003 (0)
Angles (°) (# > 4σ)	0.525 (0)	0.477 (0)	0.553 (0)
MolProbity score	1.92	1.17	1.11
Clash score	5.44	2.26	3.22
Ramachandran plot (%)			
Outliers	0.00	0.00	0.00
Allowed	3.66	2.70	1.61
Favored	96.34	97.30	98.39
Rama-Z (RMSD)			
Whole (N=423)	0.22 (0.45)	0.36 (0.43)	0.91 (0.31)
Helix (N=246)	1.21 (0.34)	0.93 (0.36)	1.40 (0.24)
Sheet (N=27)	--- (---)	0.29 (1.11)	0.69 (0.80)
Loop (N=150)	-2.18 (0.54)	-0.83 (0.50)	-0.66 (0.36)
Rotamer outliers (%)	3.23	1.11	0.57
Cβ outliers (%)	NA	NA	NA
Peptide plane (%)			
Cis-proline/general	0.0/0.0	5.0/0.0	5.0/0.0
Twisted proline/general	0.0/0.0	0.0/0.0	0.0/0.0
CaBLAM outliers (%)	1.14	0.25	0.00
ADP (B-factors)			
Iso/Aniso (#)	2,929/0	3,560/0	6,883/0
Min/max/min ($Å^2$)			
Protein	24.78/133.27/56.43	14.20/127.02/53.63	10.29/175.03/79.41
Nucleotide	---	16.39/110.65/50.88	37.22/140.26/76.70
Ligands	---	42.99/129.68/63.25	37.07/163.08/83.51

SUPPLEMENTARY METHODS

*Ec*PAP Processivity assay

A polymerase trapping method adapted from a previous study[1] was used to assess the processivity of *Ec*PAP under low-salt (50 mM NaCl) and high-salt conditions (250 mM NaCl). Three separate primer extension reactions ("control", "blocking", "assay") were carried out. **Assay:** *Ec*PAP (0.2 μM) was pre-incubated with equimolar FAM-$(rA)_{21}$ RNA ("P") in 1x processivity assay buffer (50 mM MOPS-NaOH, 50/250 mM NaCl, 10 mM $MgCl_2$, pH 7.0) in the absence of rATP to facilitate the assembly of *Ec*PAP-RNA complexes. The mixture was then spiked with excess unlabeled tRNA (0.2 mM) and rATP (0.2 mM) to initiate polyadenylation of the *Ec*PAP-bound FAM-$(rA)_{21}$ RNA. The 1000-fold excess of tRNA to FAM-$(rA)_{21}$ meant that *Ec*PAP would be kinetically hindered from further extending FAM-labeled RNA species upon even a single dissociation event. Any extension of FAM-$(rA)_{21}$ detected under these conditions could thus be interpreted as processive synthesis by *Ec*PAP.

SUPPLEMENTARY NOTES

Supplementary Note 1. *Ec*PAP-ssDNA binding and its implications

While attempting to characterize the processivity of *Ec*PAP for an unrelated project, we incidentally observed that *Ec*PAP forms a stable complex with single-stranded DNA (ssDNA) under low-salt conditions **(Supplementary Fig. 1a)**, despite rejecting it as a substrate **(Supplementary Fig. 1b)**. This, combined with the fact that the complex was salt-labile, meant that bulk binding of *Ec*PAP to polynucleotides was primarily mediated by "sugar-blind" electrostatic interactions involving the backbone phosphate moieties. However, the loss of sugar 2'-OH still had to be disruptive to the formation of a catalytically productive complex, as ssDNA evidently could not be polyadenylated under standard conditions **(Supplementary Fig. 1b)**. Discounting sugar-dependent differences in long-range backbone structures between RNA and DNA, we thought the only reasonable location where such a loss could be structurally significant would be at the primer 3' terminus. After all, the 3' terminal nucleotide is the only part of the primer directly involved in chemical catalysis (*i.e.* nucleotidyl transfer), with the rest of the bulk primer simply contributing binding affinity (already established in a "sugar-blind" manner) for the terminal nucleotide. Assuming the existence of a hypothetical hydrogen bond acceptor X in the *Ec*PAP active site, the loss of primer 3' terminal 2'-OH would disrupt the 2'-O-H···X interaction required for formation of a productive complex. Based on this hypothetical picture of primer sugar recognition in *Ec*PAP, we conjectured that a single 3' terminal deoxynucleotide substitution in an RNA primer would be functionally equivalent to using a DNA primer, abolishing *Ec*PAP activity. Below is a hand-drawn schematic of the conjectured sugar-dependent primer 3' terminal binding in *Ec*PAP from March, 2022, when the idea was first conceived of. (NT^{PAP} represents the catalytic N-terminal domain of *Ec*PAP, whereas NT^{TdT} can be thought of as a synthetic "sink" for *Ec*PAP-unbound 3'-deoxynucleotide termini.)

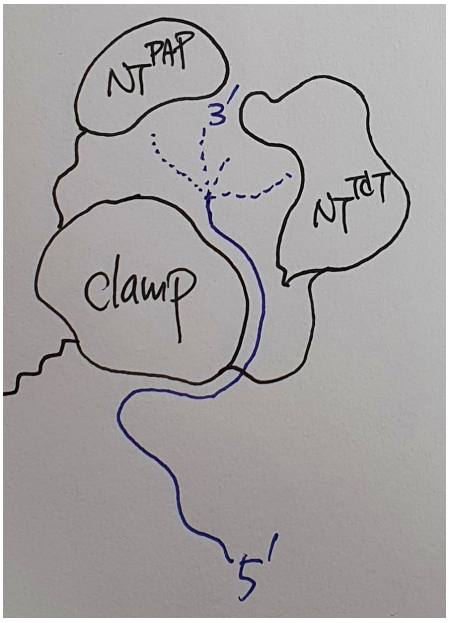

Supplementary Note 2. Intrinsic processivity in *Ec*PAP during polyadenylation

We assayed the processivity of poly(A) tail synthesis by *Ec*PAP under low-salt (50 mM NaCl) and high-salt (250 mM NaCl) conditions using a tRNA trap introduced to an otherwise normal FAM-$(rA)_{21}$ primer extension reaction **(see Supplementary Methods for detail)**. Specifically, *Ec*PAP (0.2 μM) was pre-incubated with FAM-$(rA)_{21}$ (0.2 μM) and spiked with excess tRNA (0.2 mM) and rATP (0.2 mM) to initiate poly(A) tail synthesis. The strength of the tRNA trap was such that *Ec*PAP could not re-associate with FAM-$(rA)_{21}$ upon even a single dissociation event **(Supplementary Fig. 3, "blocking" reaction)**. Note that *Ec*PAP was fully active under both low-salt and high-salt conditions tested in the experiment **(Supplementary Fig. 3, "control" reaction)**. We could thus attribute any extension in FAM-$(rA)_{21}$ to processive synthesis originating from a single binding event (*i.e.* the pre-incubation). *Ec*PAP was found to synthesize a poly(A) tail >100 nt in length onto FAM-$(rA)_{21}$ under low-salt conditions but could not at all extend FAM-$(rA)_{21}$ under high-salt conditions **(Supplementary Fig. 3, "assay" reaction)**. This meant that *Ec*PAP exhibited significant processivity of >100 nt that was fully suppressed by high ionic strength.

Supplementary Note 3. State-state kinetics for FAM-(rA)$_{20}$-dA primer utilization

Due to exceedingly slow reaction kinetics for FAM-(rA)$_{20}$-dA utilization, we were forced to employ very long reaction times (3 h, *cf.* 1 min for FAM-(rA)$_{21}$) to be able to detect the formation of any extension product. Note that increasing the concentration of *Ec*PAP (5 nM) was not an option so as to satisfy the steady-state assumption [E] << [P] (E: *Ec*PAP-rATP, P: primer). Unfortunately, this meant that we could not limit primer extension to +1 nt (*i.e.* $P \rightarrow P_{+1}$), as typically done to obtain simple steady-state kinetics $v_P = -d[P]/dt = d[P_{+1}]/dt = (k_{cat})^P[E]_0[P]/((K_m)^P+[P])$. Significant P_{+1} turnover and formation of secondary +2 nt extension product (*i.e.* P_{+2}) would make it necessary to consider the kinetics for reaction $P_{+1} \rightarrow P_{+2}$, and with steady-state assumptions violated for $P_{+1} \rightarrow P_{+2}$, it would no longer be feasible to determine $(k_{cat})^P$ and $(K_m)^P$ just from initial velocity data (*i.e.* $(v_P)_0$ vs $[P]_0$). However, in our case, the fact that P = FAM-(rA)$_{20}$-dA and P_{+1} = FAM-(rA)$_{21}$-dA-rA meant that kinetics for $P_{+1} \rightarrow P_{+2}$ was much faster than $P \rightarrow P_{+1}$, allowing us to make the following derivation below.

Reaction system (assuming distributive kinetics and full rATP occupancy in *Ec*PAP)

(1) $E+P \rightleftharpoons E\text{-}P \rightarrow E + P_{+1} + PP_i$ (very slow)

(2) $E+P_{+1} \rightleftharpoons E\text{-}P_{+1} \rightarrow E + P_{+2} + PP_i$ (fast)

We can assume standard Michaelis-Menten kinetics for reaction 1, as the condition [P] >> [E] is maintained, which means $d[P_{+1}]/dt = (k_{cat})^P[E]_0[P]/((K_m)^P+[P])$. For reaction 2, although $[P_{+1}]$ is present only at low levels (final level <20% of $[P]$), the long reaction time relative to fast kinetics effectively ensures steady-state equilibrium for the species $E\text{-}P_{+1}$, leading to $d[P_{+2}]/dt = (k_{cat})^{P_{+1}}[E]_0[P_{+1}]/((K_m)^{P_{+1}}+[P_{+1}])$. In summary,

$$v_{P_{+1}} = \frac{d[P_{+1}]}{dt} = \underbrace{\frac{(k_{cat})^P[E]_0[P]}{(K_m)^P + [P]}}_{Formation\ in\ reaction\ 1} - \underbrace{\frac{(k_{cat})^{P_{+1}}[E]_0[P_{+1}]}{(K_m)^{P_{+1}} + [P_{+1}]}}_{Consumption\ in\ reaction\ 2}$$

$$v_{P_{+2}} = \frac{d[P_{+2}]}{dt} = \underbrace{\frac{(k_{cat})^{P_{+1}}[E]_0[P_{+1}]}{(K_m)^{P_{+1}} + [P_{+1}]}}_{Formation\ in\ reaction\ 2}$$

Combining the two expressions,

$$v_{P_{+1}} + v_{P_{+2}} = \frac{d([P_{+1}] + [P_{+2}])}{dt} = \frac{(k_{cat})^P[E]_0[P]}{(K_m)^P + [P]}$$

In other words, fitting the combined formation rates for +1 and +2 nt extension products against initial primer (P) concentration yields $(k_{cat})^P$ and $(K_m)^P$ from a single experiment. Moreover, for $K_m >> [P]$ (*i.e.* when the maximum attainable primer concentration in the experiment is far below $(K_m)^P$), the model can be linearized as $d([P_{+1}]+[P_{+2}])/dt \approx (k_{cat})^P[E]_0/(K_m)^P[P]$, with the slope equal to $(k_{cat}/K_m)^P[E]_0$.

Supplementary Note 4. Challenges in cryo-EM analysis of *Ec*PAP

Single-particle cryo-EM analysis of substrate-engaged EcPAP was challenging due to salt-sensitivity, aggregation, denaturation at the air-water interface (AWI), and preferred orientation. Notably, *Ec*PAP-RNA binding was stable only under low-salt conditions (<50 mM NaCl) **(Supplementary Fig. 6a)**, while *Ec*PAP tended to aggregate and precipitate out of solution at <250 mM NaCl **(Supplementary Fig. 6b)**. We found that adding equimolar arginine and glutamate (50 mM each) (following a previous report[2]) suppressed macroscopic precipitation under the low salt conditions required **(Supplementary Fig. 6c)**, but cryo-EM imaging still revealed *Ec*PAP to form filament-like aggregates that did not yield to structure determination **(Supplementary Fig. 6c)**. After extensive rounds of screening for additives, we found that sodium sulfate (Na_2SO_4) dissolved the aggregates into single particles **(Supplementary Fig. 6d)** without compromising *Ec*PAP-RNA binding **(Supplementary Fig. 7)**. Note that other simple salts such as sodium acetate (NaOAc) did not show comparable activity **(Supplementary Fig. 6e)**. Still, data processing revealed severe preferred orientation that precluded structure determination, though we could obtain clear, high-resolution 2D class averages **(Supplementary Fig. 6f)**. We produced graphene-coated Quantifoil Au 300 1.2/1.3 grids using a polymer-assisted approach[3] **(Supplementary Fig. 6g)** and attempted data collection, but *Ec*PAP still showed severe preferential orientation **(Supplementary Fig. 6h)**. Only after adding *Aav*LEA1 peptide[4] could we obtain a sample amenable for high-resolution structure solution. Fortunately, the final optimized buffer conditions **(see Methods for detail)** produced high-quality grids that yielded isotropic, high-resolution reconstructions in a reproducible fashion **(Fig. 3, Supplementary Fig. 9-10)**.

Supplementary Note 5. Wild-type *Ec*PAP is practically incapable of dNTP incorporation

Confident in our understanding of primer terminal sugar specificity in *Ec*PAP, we attempted a *d*MIL reaction **(Fig. 1)** using wild-type *Ec*PAP with dATP. FAM-$(rA)_{21}$ (0.5 µM) was incubated with *Ec*PAP (500 nM) and excess dATP (1 mM). Surprisingly, denaturing PAGE analysis revealed a polydisperse product mixture, initially suggesting multiple dAMP incorporation **(Supplementary Fig. 13a)**. However, MALDI-TOF analysis of silica column-purified reaction products confidently identified each product species as having the form FAM-$(rA)_{20+n}$-dA (n≥0), consistent with polymerization of contaminating rATP followed by a single dAMP addition **(Supplementary Fig. 13b)**.

We measured steady-state initial velocities for rATP and dATP incorporation using FAM-$(rA)_{21}$ (2.5 µM) as primer **(Supplementary Fig. 13c-d)**. The resulting specificity constants (k_{cat}/K_m) were 4.70(±0.43)×10^4 $M^{-1}s^{-1}$ for rATP and 1.65±0.63 $M^{-1}s^{-1}$ for dATP, reflecting a ~3×10^4-fold preference for rATP **(Supplementary Fig. 13e)**. The reduced activity with dATP was primarily due to weakened binding (K_m, ~10^3-fold increase), with a modest decrease in turnover (k_{cat}, ~40-fold decrease). These values indicate that dATP would be effectively excluded in the presence of rATP. Indeed, even trace rATP contamination (<0.1%) yielded competitive incorporation, resulting in the observed product pattern **(Supplementary Fig. 13a)**.

*Ec*PAP is also highly selective for the adenine nucleobase, rejecting NTPs with non-adenine nucleobases **(Supplementary Fig. 7)**. In summary, wild-type *Ec*PAP exhibits stringent specificity for both the sugar (ribose) and nucleobase (adenine) moieties of the incoming NTP substrate. Achieving *d*MIL with all four canonical dNTPs (dATP, dTTP, dCTP, dGTP) would therefore require the simultaneous relaxation of both substrate specificities.

Supplementary Note 6. Evidence for deviating rATP pose in PDB 3AQN

Structural alignment between our stalled ternary complex structure and the previously reported crystal structure for *Ec*PAP-rATP complex (PDB 3AQN) revealed significant deviations in poses for rATP adenine, D194, and R200 **(Supplementary Fig. 15a)**. Inspection of the published coordinates and structure factors for PDB 3AQN revealed a lack of clear $2F_o$-F_c density for rATP regardless of map threshold (0.5-1.5 σ) and a strong negative difference map peak (>6.5 σ) for rATP in both *Ec*PAP chains (A and B). This indicated that there was weak experimental evidence to support the published rATP pose in 3AQN. Considering that the authors attempted to soak rATP into a pre-formed crystal of *apo Ec*PAP in their structure determination campaign[5], it is possible that rATP failed to bind stably to the *Ec*PAP active site. In fact, the conformation of R200 in 3AQN (rotamer well-defined in the $2F_o$-F_c map) is incompatible with the rATP pose **(Supplementary Fig. 15d)** in our stalled ternary complex structure, clashing with the adenine 6-NH_2 at a distance of ~1.6 Å **(Supplementary Fig. 15e)**. Combined with the published observation by the authors of PDB 3AQN that co-crystallization of *Ec*PAP was not possible under the same conditions used for *apo Ec*PAP crystal formation[5], this suggests that a conformational change (potentially corresponding to the open-to-closed change described in this Article) in *Ec*PAP is absolutely necessary for rATP binding. Furthermore, a 24 ns all-atom molecular dynamics (MD) simulation run with the PDB 3AQN *Ec*PAP-rATP complex structure as initial coordinates showed rapid dissociation of rATP from *Ec*PAP, again supporting the notion that the published structure is not physically realistic. Overall, the observations indicate that the rATP coordinates in PDB 3AQN represents a loosely-bound, non-native structure.

SUPPLEMENTARY REFERENCES

1. Washington, M.T., Johnson, R.E., Prakash, S. & Prakash, L. Fidelity and Processivity of Saccharomyces cerevisiae DNA Polymerase η. *Journal of Biological Chemistry* **274**, 36835-36838 (1999).
2. Golovanov, A.P., Hautbergue, G.M., Wilson, S.A. & Lian, L.-Y. A Simple Method for Improving Protein Solubility and Long-Term Stability. *Journal of the American Chemical Society* **126**, 8933-8939 (2004).
3. Ahn, E. et al. Batch Production of High-Quality Graphene Grids for Cryo-EM: Cryo-EM Structure of Methylococcus capsulatus Soluble Methane Monooxygenase Hydroxylase. *ACS Nano* **17**, 6011-6022 (2023).
4. Abe, K.M., Li, G., He, Q., Grant, T. & Lim, C.J. Small LEA proteins mitigate air-water interface damage to fragile cryo-EM samples during plunge freezing. *Nature Communications* **15**, 7705 (2024).
5. Toh, Y., Takeshita, D., Nagaike, T., Numata, T. & Tomita, K. Mechanism for the Alteration of the Substrate Specificities of Template-Independent RNA Polymerases. *Structure* **19**, 232-243 (2011).